# LUND UNIVERSITY

## InP/GaInP Nanowires for Tandem Junction Solar Cells

### Growth, Processing, and Characterization

Zeng, Xulu

2018

InP/GaInP Nanowires for Tandem Junction Solar Cells

ii

# InP/GaInP Nanowires for Tandem Junction Solar Cells

## Growth, Processing, and Characterization

Xulu Zeng

LUND
UNIVERSITY

DOCTORAL DISSERTATION
by due permission of the Faculty of Engineering, Lund University,
Sweden.
To be defended at the Rydberg Lecture Hall at the Department of Physics,
at 13:15, June 8th, 2018.

*Faculty opponent*
Dr. Kirsten Moselund

IBM Research Zurich

| Organization<br>LUND UNIVERSITY | Document name<br>DOCTORAL DISSERTATION |
|---|---|
| | Date of issue |
| Author(s) Xulu Zeng | Sponsoring organization |

| Title and subtitle<br>InP/GaInP Nanowires for Tandem Junction Solar Cells: Growth, Processing, and Characterization |
|---|

**Abstract**

Semiconductor nanowire solar cells have achieved comparable efficiency to their planar counterparts with substantial reduction of material consumption. Tandem geometry is a path towards even higher efficiency. However, extensive studies are needed to reach this goal. My study started from the building blocks of the materials used in the upper cell, namely GaInP nanowires. The growth and doping control was the focus. We achieved well-controlled GaInP nanowire arrays and effective doping control of both $n$-type and $p$-type which is needed for use in the tandem junction solar cells.

In a tandem junction solar cell, a tunnel junction which is virtually a degenerately doped $pn$-junction is a critical component. It provides the connection between adjacent subcells with low-resistivity and optical-transparency. With the knowledge obtained from our doping evaluation studies, we established the growth of InP/GaInP heterojunction nanowires with degenerate doping achieved at the material heterointerface which is the prerequisite for the tunneling effect. The tunnel diodes were realized in both forward (InP/GaInP) and reverse (GaInP/InP) directions. This enabled the tandem structures in the forward (InP subcell (bottom)/GaInP subcell (top)) and reverse (GaInP subcell (bottom)/InP subcell (top)) direction. (To enable the use of the reverse tandem structure, peel-off of the nanowires is needed since the higher-bandgap GaInP subcell should be on the top of the tandem structure in applications.)

When the tunnel junction is incorporated into multiple $pn$-junction structures, the growth of the complex structure can bring extra influence to the entire device performance due to the VLS growth mechanism of nanowires. To simplify the diagnostics of tandem junction structures, we designed a test structure which connects a tunnel junction back to back with a $p$-$i$-$n$ junction (namely a '$n$-$pin$' structure). The $n$-$pin$ structure has both ends of $n$-type, facilitating Ohmic contact formation. We found that a strong memory effect from the firstly-grown segment can non-intentionally dope the following segments. To overcome this challenge, compensation doping will probably be needed.

The transfer of large area nanowire arrays to cheap substrates can significantly reduce the material cost. We developed an effective technology to embed the nanowire arrays into a polymer film and peel the film off from the native substrate.

These studies pave the way to the realization of the first InP/GaInP nanowire tandem junction solar cell. The peel-off technique will also be of broad interests for reducing the fabrication cost of other nanowire devices, such as light emitting diodes and photodetectors.

| Key words<br>nanowires, GaInP, InP, tandem, tunnel diode, solar cell |
|---|

| Classification system and/or index terms (if any) |
|---|

| Supplementary bibliographical information | Language: English |
|---|---|

| ISSN and key title | ISBN<br>978-91-7753-716-8 (print)<br>978-91-7753-717-5 (pdf) |
|---|---|

| Recipient's notes | Number of pages | Price |
|---|---|---|
| | Security classification | |

I, the undersigned, being the copyright owner of the abstract of the above-mentioned dissertation, hereby grant to all reference sources permission to publish and disseminate the abstract of the above-mentioned dissertation.


Signature _____ Date: 2018-05-01 _____

# InP/GaInP Nanowires for Tandem Junction Solar Cells

## Growth, Processing, and Characterization

Xulu Zeng

**LUND UNIVERSITY**

MILJÖMÄRKT
3041 0903
MADE IN SWEDEN

ISO 14001:2004
CERTIFICATION
TM
Intertek

Media-Tryck is an environmental-
ly certified and ISO 14001 certified
provider of printed material.
Read more about our environmental
work at www.mediatryck.lu.se

*To my parents*

# Table of Contents

x

# Abstract

Semiconductor nanowire solar cells have achieved comparable efficiency to their planar counterparts with substantial reduction of material consumption. Tandem geometry is a path towards even higher efficiency. However, extensive studies are needed to reach this goal. My study started from the building blocks of the materials used in the upper cell, namely GaInP nanowires. The growth and doping control was the focus. We achieved well-controlled GaInP nanowire arrays and effective doping control of both *n*-type and *p*-type which is needed for use in the tandem junction solar cells.

In a tandem junction solar cell, a tunnel junction which is virtually a degenerately doped *pn*-junction is a critical component. It provides the connection between adjacent subcells with low-resistivity and optical-transparency. With the knowledge obtained from our doping evaluation studies, we established the growth of InP/GaInP heterojunction nanowires with degenerate doping achieved at the material heterointerface which is the prerequisite for the tunneling effect. The tunnel diodes were realized in both forward (InP/GaInP) and reverse (GaInP/InP) directions. This enabled the tandem structures in the forward (InP subcell (bottom)/GaInP subcell (top)) and reverse (GaInP subcell (bottom)/InP subcell (top)) direction. (To enable the use of the reverse tandem structure, peel-off of the nanowires is needed since the higher-bandgap GaInP subcell should be on the top of the tandem structure in applications.)

When the tunnel junction is incorporated into multiple *pn*-junction structures, the growth of the complex structure can bring extra influence to the entire device performance due to the VLS growth mechanism of nanowires. To simplify the diagnostics of tandem junction structures, we designed a test structure which connects a tunnel junction back to back with a *p-i-n* junction (namely a '*n-pin*' structure). The *n-pin* structure has both ends of *n*-type, facilitating Ohmic contact formation. We found that a strong memory effect from the firstly-grown segment can non-intentionally dope the following segments. To overcome this challenge, compensation doping will probably be needed.

The transfer of large area nanowire arrays to cheap substrates can significantly reduce the material cost. We developed an effective technology to embed the nanowire arrays into a polymer film and peel the film off from the native substrate.

These studies will pave the way to the realization of the first InP/GaInP nanowire tandem junction solar cell. The peel-off technique will also be of

broad interests for reducing the fabrication cost of other nanowire devices, such as light emitting diodes and photodetectors.

# Popular science summary

Solar energy, which reaches our earth every day, corresponds to 15000 times more than all the electricity we need in our daily lives. We can overcome our great challenge in finding alternative sources of energy for oil, coal, and gas if we were able to capture the sun's rays in smarter ways. At NanoLund at Lund University, extremely thin and incredibly small nanowires that are less than 1% of the thickness of a hair are manufactured. Nanotechnology, which has many uses that can change our everyday life in the future, is about controlling small materials down to the atomic level. NanoLund is one of the most advanced nanoscience centers in the world when it comes to taking advantage of the nanomaterials' properties and producing nanomaterials in a cheap and efficient manner.

I have been involved in the manufacturing of semiconductor nanowires. Semiconductors are used in most types of solar cells today and are the type of material that can convert light into electricity. The researchers at LU previously held the record efficiency of nanowire solar cells of 13.8 %. The nanowire arrays covered only about 10 % of the surface that the conventional solar cells need. That was a big leap from the former record (5 %) and has attracted the world's attention from both academia and industry. Recently, we have updated the efficiency of our devices to 15 %. So far, our solar cells consist of one single $pn$-junction in dense nanowire arrays (about 4 million/mm$^2$). However, the single junction can only harvest a limited range of the solar energy, therefore a single-junction solar cell has a limited efficiency roof.

In order to move forward, our next goal is to introduce the tandem junction design into nanowires, which is the strategy used in the most efficient solar cells of all kinds. In a tandem junction solar cell, several junctions are connected in series so that different parts of the solar spectrum can be more efficiently harvested by each junction. A design of the GaInP/InP double junction solar cell is predicted to increase the efficiency to above 35 %.

I have also been striving to transfer nanowires from the substrate where they were grown to another foreign substrate which can be cheaper materials like silicon, glass or plastic by embedding the nanowires in a polymer film. A polymer film of nanowire devices will be light in weight and flexible in shape. As one is no longer locked to only silicon wafers, which are the standard base for building a solar cell, the applications for a flexible device become broader. The nanowire film can be conveniently applied on different surfaces, such as building sidewalls, mobile electronics, and wearable devices. With this "cut and paste" technique of nanowires, the cost of devices will be further lowered by reuse of the substrate for nanowire growth.

The price of solar cells has been reduced a lot in the past 20 years and is now competitive with other energy resources. With the recent progress from binary-material nanowires to ternary-material nanowires, a more advanced nanowire tandem junction solar cell becomes possible. As Laozi said:" the Way begets one; one begets two; two begets three; three begets myriad creatures.", we are optimistic that the next generation solar cells will promisingly power our future by solar energy, which is free, endless and environmentally friendly!

-Excerpt and revised from the interview of me for the popular science article "The sunhunters – with knowledge to collect the light" on the magazine of "Mission is Possible".

# Acknowledgments

My Ph.D. period is an unforgettable experience that I will always treasure. The work of this thesis is achieved with the concern and help from my supervisors, my colleagues, and my friends.

Firstly, I would like to express my deepest gratitude to my supervisors, Professor Magnus T. Borgström, Professor Lars Samuelson, and Professor Reine Wallenberg. You provide me the great opportunity to work on this exciting project and lead me into the area of nanoscience. My main supervisor, Magnus, I admire your expertise and efficiency very much. Your meticulous attitude towards science is always the best model to me. You always guide me patiently. From Lars, I get many valuable insights from a high level. Your brilliant thoughts stimulate my interest in my studies. You are always amiable and easy of approach. Reine, you lead me to the world of electron microscopy which was entirely new to me. I am very moved and grateful for your considerate help!

Then, I would like to thank the members of the group for your help in all aspects of my life. Magnus, Alexander, Gaute, Vilgailė, and Lukas, many thanks for the excellent teamwork! Enrique, Pyry, and Yuwei, thanks a lot for your support, and I have learned a lot from the collaboration with you! I wish all of you a bright future!

In the long march of the studies I have been working on, I want to express my gratitude to my collaborators: Arkady, Nicklas, Jesper, Mats-Erik, Håkan, Rainer, Claes, Niklas, Wei, Olof, Yang, Reza, Fredrik, Jovana, Mohammad, Ville, Steven, Andrea, Xianshao, Lert, Xiaojun, Renato, Hanna, and Marina.

I also get firm support from other professors and colleagues: Peter, Martin, Bi, Kimberly, Sebastian, Jonas, Christelle, Carina, Fangfang, Ali, Vishal, Johannes, Elvedin, Cezar, Karl, Jason, and Stefan.

In everyday life, my officemates: Vilgailė, Artis, Marcus, I-Ju, and Trung, together create a warm and friendly environment. We had many interesting scientific discussions, sharing of knowledge and experience.

My FTF colleagues who have helped with my life both in and out of work, including Rong, Zhen, Neimantas, Chunlin, Taiping, Yadan, Laura, David, Frida, Sudarkha, Zeng-Zhao, Robert, Bao, Florinda, Beckmurat, Malin, and Kushagr. Thanks for your kindness!

I would like to thank Ingvar, Damir, and Christian from SolVoltaics for your help!

# List of papers

This thesis is based on the following articles:

I. **In$_x$Ga$_{1-x}$P nanowire growth dynamics strongly affected by doping using diethylzinc**

G. Otnes, M. Heurlin, <u>X. Zeng</u>, and M. T. Borgström

*Nano Letters*, **2017**, *17* (2), 702-707.

I grew, processed and measured the nanowire tunnel diode samples. I contributed to the writing of the article.

II. **Electrical and optical evaluation of *n*-type doping in In$_x$Ga$_{(1-x)}$P nanowires**

<u>X. Zeng</u>*, R. T. Mourão*, G. Otnes*, O. Hultin, V. Dagytė, M. Heurlin, and M.T. Borgström

*These authors contributed equally.

*Nanotechnology*, **2018**, *29*, 255701.

I coordinated the experiments and shared the main responsibility for writing this article. I jointly analyzed the measurement results.

III. **InP/GaInP nanowire tunnel diodes**

<u>X. Zeng</u>, G. Otnes, M. Heurlin, R. T. Mourão, and M. T. Borgström

*Nano Research*, **2017**, doi: 10.1007/s12274-017-1877-8.

I developed the growth, processed and performed the electrical measurement of the samples. I also performed the SEM and TEM measurements on the samples. I analyzed the results and wrote the main part of the article.

IV. **Growth and optimization of GaInP/InP nanowire tunnel diode**

<u>X. Zeng</u>, G. Otnes, M. Heurlin, and M. T. Borgström

*Proceedings of the 44$^{th}$ IEEE Photovoltaic Specialists Conference, 2017*

I grew the samples, took the SEM images and analyzed the EBIC measurement data together with the coauthors. I was the main responsible for writing the article.

V.     **Carrier recombination processes in gallium indium phosphide nanowires**

W. Zhang*, X. Zeng*, X. Su, X. Zou, P. -A. Mante, M. T. Borgström, and A. Yartsev

*These authors contributed equally.

*Nano Letters*, **2017**, *17* (7), 4248-4254.

I participated in the design of the experiments. I grew the samples, took the SEM images, performed the XRD measurements, peeled and transferred the nanowires into a polymer film, and performed the TEM measurements. I jointly wrote the manuscript.

The following articles, listed in chronological order, are not included since they deal with topics beyond the scope of the thesis or are manuscripts not yet accepted:

VI.     **In situ surface passivation of GaInP nanowires by use of radially grown AlInP shells**

X. Zeng, W. Zhang, A. Yartsev, and M. T. Borgström

In writing.

VII.     **Diagnostics of nanowire tunnel diodes for InP/GaInP tandem junction solar cells**

X. Zeng, E. Barrigón, G. Otnes, P. Kivisaari, and M. T. Borgström

In writing.

VIII.     **Absorption and transmission of light in III-V nanowire arrays for tandem solar cell applications**

N. Anttu, V. Dagytė, X. Zeng, G. Otnes, and M. T. Borgström

*Nanotechnology*, **2017**, *28*, 205203.

IX.   Time-resolved photoluminescence characterization of GaAs nanowire arrays on native substrates

V. Dagytė, W. Zhang, X. Zeng, M. Heurlin, G. Otnes, N. Anttu, and M. T. Borgström

*Nanotechnology*, **2017**, *28*, 505706.


X.   Growth kinetics of $Ga_xIn_{(1-x)}P$ nanowires using triethylgallium as Ga precursor

V. Dagytė, M. Heurlin, X. Zeng, and M. T. Borgström

Submitted to *Nanotechnology*


XI.   Intersubband quantum disc-in-nanowire photodetectors with normal-incidence response in the long-wavelength infrared

M. Karimi, M. Heurlin, S. Limpert, V. Jain, X. Zeng, I. Geijselaers, A. Nowzari, Y. Fu, L. Samuelson, H. Linke, M. T. Borgström, and H. Pettersson

*Nano Letters*, **2018**, *18*(1), 365–372.


XII.   Effect of HCl etching on carrier recombination processes in InP nanowires

X. Su, X. Zeng, H. Němec, X. Zou, W. Zhang, M. T. Borgström, and A. Yartsev

In writing.


XIII.   Nanobeam X-ray fluorescence measurements of in situ Zn-doped nanowires reveals gradients and background doping

A. Troian, G. Otnes, X. Zeng, L. Chayanun, V. Dagytė, S. Hammarberg, D. Salomon, A. Mikkelsen, M. T. Borgström, and J. Wallentin

In writing.

# Abbreviations

| | |
|---|---|
| AlInP | aluminium indium phosphide |
| Au | gold |
| cAFM | conductive atomic force microscopy |
| CBE | chemical beam epitaxy |
| $Cp_2Mg$ | bis-cyclopentadienyl magnesium |
| DEZn | diethylzinc |
| DJSC | double junction solar cell |
| EBIC | electron beam induced current |
| EBL | electron beam lithography |
| EDX | energy dispersive X-ray spectroscopy |
| $E_g$ | energy bandgap |
| FC | First Contact polymer |
| Ga | gallium |
| GaInP | gallium indium phosphide |
| GaN | gallium nitride |
| GaP | gallium phosphide |
| $H_2$ | hydrogen |
| HBr | hydrogen bromide |
| HCl | hydrogen chloride |
| $H_2S$ | hydrogen sulfide |
| In | indium |
| InP | indium phosphide |
| ITO | indium tin oxide |
| I-V | current-voltage |
| MBE | molecular beam epitaxy |
| MOVPE | metal organic vapor phase epitaxy |
| NIL | nanoimprint lithography |

| nm | nanometer ($10^{-9}$ meters) |
|----|------|
| ns | nanosecond |
| PL | photoluminescence |
| PDMS | polydimethylsiloxane |
| $PH_3$ | phosphine |
| PMMA | polymethyl methacrylate |
| ps | picosecond |
| PVCR | peak to valley current ratio |
| RIE | reactive ion etching |
| Se | selenium |
| SEM | scanning electron microscopy |
| Sn | tin |
| STEM | scanning transmission electron microscopy |
| S1813 | microposit S1813 photoresist |
| TA | fs-transient absorption |
| Te | tellurium |
| TEM | transmission electron microscopy |
| TESn | tetraethyltin |
| TJ | tunnel junction |
| TJSC | tandem junction solar cell |
| TMIn | trimethylindium |
| TMGa | trimethylgallium |
| TRPL | time-resolved photoinduced luminescence |
| TRTS | time-resolved THz spectroscopy |
| TU7 | Obducat TU7 UV curable resist |
| VLS | vapor-liquid-solid |
| VSS | vapor-solid-solid |
| WZ | wurtzite |
| XRD | X-ray diffraction |

XRF        X-ray fluorescence

ZB         zincblende

Zn         zinc

µm         micrometer ($10^{-6}$ meters)

# 1. Introduction

In 2016, the landmark Paris agreement came into force, addressing the urgent needs on limiting the climate changes. In this historical agreement, countries came together and agreed to work to control the global temperature rise to well below 2 °C above pre-industrial levels [1]. As a non-renewable resource, the conventional fossil fuels with their high emissions of $CO_2$ will eventually step down from the stage of history. Any alternative energy sources should fulfill the requirements of consistently sufficient power supply and eco-friendly fabrication, storage, and usage. Tracing their roots, most energy resources, including fossil fuels, biomass energy, hydroelectric, and wind energy, originate from solar energy. The total annual solar radiation falling on the earth's surface is an order of magnitude greater than all the estimated non-renewable energy resources and about 14000 times of the world's total annual energy consumption in 2015 [2]. As the permanent and most abundant resource on earth, solar energy is capable of de-carbonizing the global economy and becoming the ultimate energy solution for the 21st century.

There are many techniques exploiting the big energy treasure of solar energy. They store the solar energy into different forms of energy. For example, photovoltaics (PV) converts sunlight into electricity [3]; artificial photosynthesis converts solar energy into chemical energy, such as photocatalytic water splitting [4] and solar carbon dioxide fixation [5]; solar thermal conversion harnesses solar energy to generate thermal energy or electricity, such as solar water heating [6] and concentrated solar thermal electric generation, respectively [7]. According to the second law of thermodynamics, a direct energy transformation/transition from solar energy to the type of energy that is to be used is the most efficient way, i.e. without any loss via an intermediate third form of energy. Fitting well with this electrified world, a solar cell, also called a photovoltaic cell, is a device that converts solar radiation directly into electricity. The photovoltaic effect was first reported by Edmund Becquerel in 1839 [8]. The first solid-state solar cell was invented by Charles Fritts in 1883 by coating selenium with a layer of gold to form the junction. However, the practical development in solar cells began in the 1950s when scientists at Bell Telephone discovered that silicon *pn*-junction created an electric charge when exposed to sunlight [3]. With a vast

government support, academic research, and industry investment, there has been a huge growth in worldwide solar PV power, exceeding 400 GW at the end of 2017 [9]. Meanwhile, a dramatical decrease of solar cell price has taken place in the recent decades, from approximately 76.7 USD/W in 1977 to 0.2 USD/W in 2018 [10]. The World Energy Council´s report anticipates that the photovoltaic systems could generate 16 % of the world´s total power by 2050 [11]. However, although having experienced a huge growth, the PV power produces only about 2 % of all electricity used globally today [10]. One of the main obstacles preventing the large-scale implementation of solar PV power is the inefficiency of devices.

On the one hand, crystalline and polycrystalline silicon solar cells dominate the conventional PV industry. In the last ten years, the average efficiency of commercial wafer-based Si solar cell modules has increased from about 12% to 17 % [12], while the record lab-scale Si cells can reach an energy conversion efficiency of 26.7 % (monocrystalline) [13]. Theoretically, the upper limit efficiency for Si solar cells is 29 % [14]. Nevertheless, the reason for the limitted efficiency of Si solar cells is the indirect and rarely tunable bandgap of Si, which is only able to harvest a limited amount of solar radiation. The rest of it either passed through without being absorbed or is lost as heat. On the other hand, III-V compound semiconductors have a wide range of adjustable direct bandgaps and thus have a better coverage of the solar spectrum. The record GaAs solar cell has achieved an efficiency of 28.8 % (1 sun, AM1.5) [13]. Furthermore, by stacking these materials in series, the combination of several optimal bandgaps can more efficiently harvest the sunlight with wider coverage of the solar spectrum and less thermalization loss, compared to a single bandgap material. Therefore, the total efficiency can be summed up from each subcell. This is the so-called tandem junction (or multi-junction) solar cell, which holds the world record of 46 % (508 suns) among all current types of solar cells [15]. However, since large active areas are necessary due to the low energy density of sunlight on earth [16], the difficulties in combining III-V materials with the mainstream Si platform [17] and the cost of the expensive III-V materials are important factors that limit their terrestrial applications [18].

To lower the cost of III-V solar cells, one can either engineer the sunlight to match the absorption of the solar cell or engineer the light-absorbing materials to match the solar spectrum. In the first route of engineering the sunlight, one way is to concentrate a large area of the incident light so that the energy density per unit area increases. Consequently, the required amount of material can be reduced. The drawbacks of this route include that additional cost will be spent on the construction and installation of light integrating systems, and that the device fabrication complexity will also increase. In the second route of

2

engineering the light-absorbing materials, materials with better optical properties and low consumption can be designed and manufactured. Additionally, lift-off of the epitaxial materials and recycle of the thick III-V substrates (the base for material growth) can effectively reduce material consumption [19]. Alternatively, the use of expensive III-V substrates can be avoided via direct growth of III-V materials on relatively cheap Si substrates. However, there are challenges in obtaining high-quality materials due to the large lattice mismatch between the Si substrate and the III-V epitaxial layers [20].

Thanks to the rapid development of nanotechnology in the recent decades, now ordered nanomaterials can be fabricated in large scale [21][22][23]. III-V semiconductor nanowires are rod-like semiconductors with a diameter of nanometer scale. A typical nanowire can be several to hundreds of nanometers in diameter and several to tens of micrometers in length. With the progress in the growth of nanowire heterostructures and doping evaluation, the state-of-art technology opens the opportunity to fabricate nanowire solar cells where a large number of materials can be saved due to the strong light absorption enhancement by the use of ordered nanowire arrays [24]. Another benefit of the small size and high aspect ratio of nanowires is the ease of lattice matching requirement. The strain between materials with lattice mismatch can be accommodated by the large nanowire surface. Therefore, it is possible to grow more optimal material combinations for light absorption. With a rather short history of nanowire solar cells, a rapid increase of power conversion efficiency has been achieved, with the latest record of 17.8 % [25]. Compared to a similar achievement which took about half a century for Si planar technology, III-V nanowire solar cells are showing great potential to meet the requirements for solar cells for the future.


# 1.1 Principles of solar cells

A semiconductor solar cell is most commonly comprised of a *pn*-junction where a built-in electric field, generated at the *pn*-junction interface, separates the electron-hole pairs generated by the material absorbing the incident photons. This is the so-called photovoltaic effect. As long as the excess carriers can diffuse to the contacts before they recombine, they contribute to generating a photovoltage. The *p-i-n* junction is a commonly-seen design where an intrinsic segment is grown sandwiched between the *p*-type and *n*-type segment, prolonging the length of the built-in electrical field. In this prolonged built-in electrical field, more photogenerated electron-hole pairs can be collected and

contributes to the photocurrent. Thus, a higher photocurrent is usually expected in a *p-i-n* junction than that of a *pn*-junction, which in its turn can affect the photovoltage.


# 1.2 Nanowire solar cells

With the ability to fabricate nanowire heterostructures and dope the nanowires, it becomes possible to form *pn*-junctions in nanowires. Due to the free dimension, there are two types of *pn*-junction geometries that can be formed in a nanowire, i.e. an axial *pn*-junction along the nanowire axis, and a radial junction at the interface of the concentric core-shell structure. Radial junctions are predicted to potentially achieve high efficiency due to its advantage of decoupling the light-absorption direction and the charge separation direction [26]. However, in reality, there are difficulties associated with forming high-quality radial junctions [27]. Instead, axial junctions currently hold the record efficiency of nanowire solar cells.

As aforementioned, tandem junction solar cells have the ability to achieve higher efficiency than a single *pn*-junction. Therefore, it is advantageous to introduce tandem junction designs to nanowire solar cells. However, there are some challenges to overcome: (1) doping control and evaluation of nanowires; Dopants can affect nanowire growth, and the doping level in nanowires can be different from that in planar growth because of the very different growth and dopant incorporation mechanism in nanowires [28]. (2) the formation of nanowire heterostructures; due to the VLS growth mechanism, the formation of heterostructures can affect the nanowire growth direction owing to the different surface energy of different materials [29]. (3) the device characterization of complex nanowire heterostructures; the characterization techniques on nanowires are less mature than that of thin films, hence further development is needed.

There have been several reports so far on nanowire tandem junction solar cells, including tandem junctions formed in InP nanowires [30], Si nanowires [31], and a GaAs-nanowire-on-planar-Si tandem junction solar cell [32]. However, an optimal combination of heterostructure materials is needed to match the solar spectrum for high efficiency. Theoretical calculations solving the full three dimensional Maxwell equations for absorption in an $InP/Ga_{0.3}In_{0.7}P$ nanowire tandem junction solar cell predicts a maximum efficiency of 38.5% (with different nanowire diameter optimized for each subcell) or 35.5% (with uniform nanowire diameter for all subcells) [33]. The band structure of a tandem junction solar cell is shown in Figure 1.
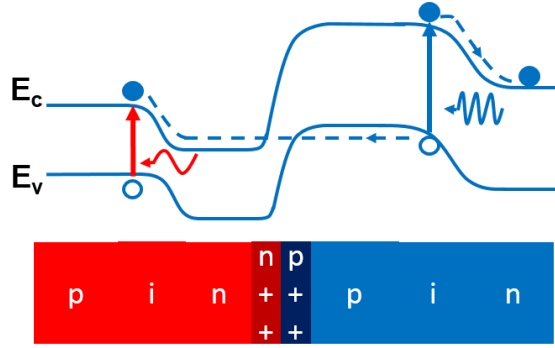
**Figure 1.** Schematic of the band structure of a tandem junction solar cell. The high-energy photons (indicated by blue color) are absorbed in the top cell with large bandgap. The low-energy photons (indicated by red color) are transmitted through the top cell and absorbed by the bottom cell with small bandgap. The connection between the top cell and the bottom cell is the tunnel junction where the electrons tunnel from the conduction band of the *n*-side of the bottom cell to the valence band of the *p*-side of the top cell.

This thesis is a study of growth, processing, and characterization of nanowires for the development of InP/GaInP nanowire tandem junction solar cells. Specifically, the thesis includes the growth and evaluation of doped GaInP nanowires, the demonstration of InP/GaInP nanowire tunnel diodes, the diagnostics of tunnel diodes embedded in a complex structure, and the development of the peel-off technique.

The structure of the thesis is as follows:

The introductory chapters will give a general introduction to the related articles involved in this thesis. First, Chapter 2 will introduce the basic material parameters of the InP-GaInP material system. Then, Chapter 3 will give the technical background of nanowire growth, processing, and characterization. The following Chapter 4 will describe the pathway and milestones by which we move from a binary nanowire solar cells towards a hybrid-binary-and-ternary tandem junction solar cell, including doping evaluation, tunnel junction realization, a test structure for diagnostics of a combination of a tunnel junction and a *p-i-n* junction. Then, Chapter 5 will discuss the peel-off technique for reducing the fabrication cost of nanowire devices. Finally, Chapter 6 will present a summary and outlook of the thesis.

5

6

# 2. InP-GaInP material system

Indium phosphide (InP) is a widely used III-V material in electronic and optoelectronic devices such as transistors, microwave devices, solar cells, light emitting diodes, and lasers [34]. InP has a direct bandgap of approximately 1.35 eV at room temperature with zincblende (ZB) crystal structure in planar growth [35]. However, due to different growth conditions and mechanism, InP with wurtzite (WZ) structure also exists in nanowires, which has a bandgap of 1.42 eV [36].

The ternary material gallium indium phosphide (GaInP) has a lattice constant that can be interpolated from the parameters of the binary material InP and gallium phosphide (GaP) by the Vegard's law:

$$a_{Ga_xIn_{1-x}P} = x\, a_{GaP} + (1-x)\, a_{InP} \qquad (2.1)$$

where a is the lattice constant of the respective materials, and $x$ is the composition of Ga in $Ga_xIn_{1-x}P$. $Ga_xIn_{1-x}P$ has an adjustable bandgap between InP (1.35 eV) and GaP (2.26 eV). Since InP has a direct bandgap and GaP has an indirect bandgap, the ternary $Ga_xIn_{1-x}P$ ($x < 0.71$) has a direct bandgap where the $\Gamma$-band dominates [37], and an indirect bandgap ($x > 0.71$) where the X-band dominates. The bandgap of $Ga_xIn_{1-x}P$ with a direct bandgap can be given by:

$$E_{g\ Ga_xIn_{1-x}P} = x\, E_{g\ GaP} + (1-x)\, E_{g\ InP} - x(1-x)b \qquad (2.2)$$

where b is the bowing parameter, which accounts for the deviation from the linear relationship between ternary material and the interpolation of binary material bandgaps. A typical value for b is 0.5 eV for the $\Gamma$-band at 300 K [38]. In Paper V, the equation for calculating the $Ga_xIn_{1-x}P$ bandgap is [39]:

$$E_{g\ Ga_xIn_{1-x}P} = 1.340 + 0.668x + 0.758x^2 \text{ (eV)} \qquad (2.3)$$

The band alignment between $Ga_xIn_{1-x}P$ and InP is type I ($x < 0.2$) [40]. The band offset ratio ($\Delta E_c/\Delta E_g$) for InP/$Ga_xIn_{1-x}P$ of 0.36 was used in Paper III [41]. Note that it has been possible to grow WZ GaP nanowires [42][43], and it is predicted that WZ GaP has a direct bandgap [44][45][46]. Therefore, the turning point from direct to indirect bandgap for $Ga_xIn_{1-x}P$ nanowires could be different from that in planar $Ga_xIn_{1-x}P$.

# 3. Nanowire growth, processing, and characterization

In this chapter, the main methods and techniques used for nanowire synthesis, device fabrication, and material and device characterization will be introduced. The nanowire growth starts from the gold particle arrays defined by nanoimprint lithography, gold evaporation, and lift-off. In the device fabrication, as-grown nanowires are broken from the native substrate and transferred to a dedicated silicon substrate. Metal contacts are evaporated on individual nanowires for electrical measurements. The electrical measurements of single nanowire devices were performed in dark and under illumination. The characterization techniques on material composition, nanowire morphology, crystal structure, and optical properties of as-grown nanowires will be described.

## 3.1 Nanowire growth

For III-V nanowire growth, there have been many techniques reported, such as chemical beam epitaxy (CBE) [47], molecular beam epitaxy (MBE) [48], aerotaxy [23], metal organic vapor phase epitaxy (MOVPE) [49], thermal evaporation [50], laser-assisted catalytic growth [51] and solution phase synthesis [52]. In general, MBE has a relatively low growth rate in order to have an atomically precise material supply. Aerotaxy, as a recently-invented technique, has the main advantage of substrate-free growth and relatively high growth rate. However, this technique is still under development with challenges in growing well-controlled $pn$-junctions and sharp heterostructures [53].

As a comparison, MOVPE has a medium growth rate. It is a method which has been intensively investigated and widely used in industrial production of III-V materials. There are many advantages of using MOVPE, including high purity, simple reactor, growth uniformity, large-scale production, selective growth, and in situ monitoring. The first MOVPE growth study dates back to

the 1960s [54]. After experiencing an intensive development during the 1970 - 1980s, MOVPE technique has become capable of producing high-quality materials with nearly atomically abrupt interfaces. Versatility and suitability of large-scale production made MOVPE the mainstream III-V semiconductor growth technique. A simple schematic of a MOVPE system is shown in Figure 2, which contains the main components including gas mixing system, source bubblers, mass flow controllers (MFCs), reactor, heaters, in situ monitoring equipment, exhaust gas line, pumping system and scrubber for exhaust gases.
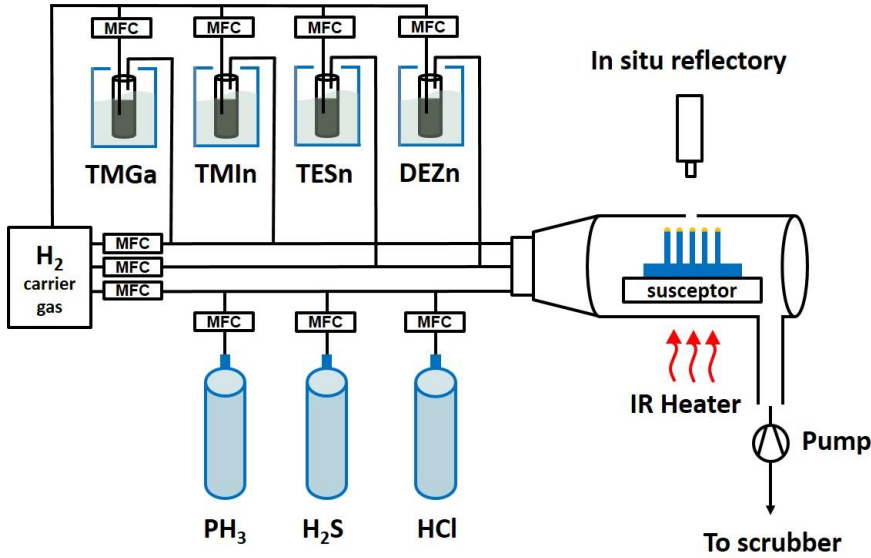


**Figure 2.** A simple schematic of a MOVPE system.

In a MOVPE growth, due to the gas phase expansion, a difference in chemical potential arises between the gas phase and the substrate surface, which in its turn leads to diffusion of precursor species from the gas phase with a high concentration towards the substrate. This is the diffusion process. Then, through surface reactions, the material reaching the growth front incorporates into the solid crystal and further reduces the chemical potential of the species. Depending on the relative chemical potential drop between the diffusion process ($\Delta\mu_D$) and the surface reactions ($\Delta\mu_S$), the two-step chemical potential drop determines the growth process is either mass-transport limited (if $\Delta\mu_D \gg \Delta\mu_S$) or kinetically limited (if $\Delta\mu_S \gg \Delta\mu_D$) [54]. For nanowire growth, it is often performed in the kinetically-limited regime because the mass-transport regime usually has a temperature more favorable for planar growth instead of nanowire growth [55]. This means that the nanowire growth is strongly dependent on the growth temperature. This is especially influential to the

growth of ternary GaInP nanowires, since it involves the complexity of low temperature precursor pyrolysis and the relative diffusion rates of growth species from the gas phase and surfaces to the growth front [56].

In general, the key parameters of MOVPE growth are growth temperature, reactor pressure, gas flows, and V/III ratio. There are highly complex processes involved, including thermodynamics, mass and heat transport, physical surface processes, chemical reactions, and subsurface processes. For example, in the growth of GaInP, the standard group III precursors are metal atoms with methyl groups such as trimethylindium (TMIn) and trimethylgallium (TMGa), and the group V precursor is phosphine ($PH_3$). In the reactor, the precursors are transported by a carrier gas ($H_2$ or $N_2$) to the heated substrate in the reactor. In the gas phases, a partial pyrolysis of the precursors takes place. The degree of pyrolysis depends on the binding energies of the molecule, temperature, and total reactor pressure. The hydrides are mainly heterogeneously decomposed on the substrate surface. The overall simplified reaction of the growth of $Ga_{0.5}In_{0.5}P$ (as an example) can be written as:

$$Ga(CH_3)_3 \text{ (g)} + In(CH_3)_3 \text{ (g)} + 2PH_3 \text{ (g)} = 2Ga_{0.5}In_{0.5}P \text{ (s)} + 6CH_4 \text{ (g)}$$
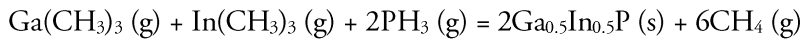
### 3.1.1 Growth of nanowire arrays

To favor the nanowire growth rather than the planar growth, a small seed particle of metal is usually used as a catalyst which can lower the nucleation barrier compared to that for the corresponding planar growth [57]. In our studies, the nanowires are grown from patterned gold particles, which are prepared by nanoimprint lithography [58]. The gold particle arrays are in a hexagonal pattern, with an average diameter of 200 nm and a thickness of approximately 65 - 70 nm, as shown in Figure 3.
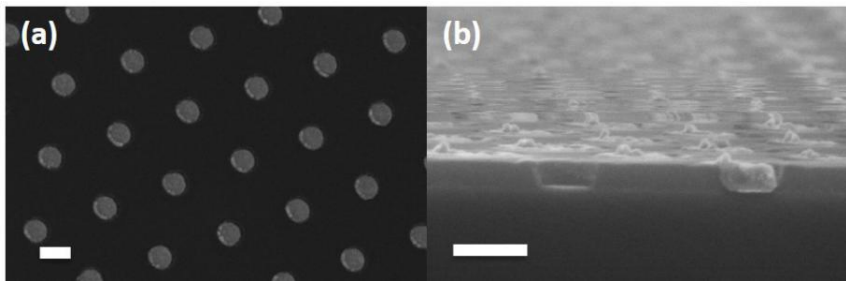


**Figure 3.** A hexagonal pattern of gold particles made by nanoimprint lithography. (a) Top view, with 0° tilt. (b) Cross-section view. The scale bars are 200 nm.

The particle-assisted nanowire growth is generally believed to be a Vapor-Liquid-Solid (VLS) process [57], even though other processes have been observed, e.g. Vapor-Solid-Solid (VSS) process [59][60]. When the group III and group V precursors are introduced into the reactor, pyrolysis of the precursors starts. The mass transport is either via a route of Vapor-Solid or Vapor-Liquid-Solid. The Vapor-Solid route is a direct impingement of adatoms from the vapor phase to the nanowire growth front (solid). As for the Vapor-Liquid-Solid route, the adatoms (vapor) are absorbed in the seed particle (liquid) and supersaturate the particle. Then, III-V nanowires crystallized underneath the seed particle, with the combination of the group V adatoms which are mainly from the vapor-solid route. A schematic of the VLS growth mechanism is shown in Figure 4. With the different mechanism of the nanowire growth compared to that of the planar growth, a new phenomenon arises, i.e. the polytypism in nanowires. This means that the crystal structure in nanowires can be a mix of WZ and ZB [61][62][63]. By contrast, ZB is normally observed for most III-V materials in planar growth.
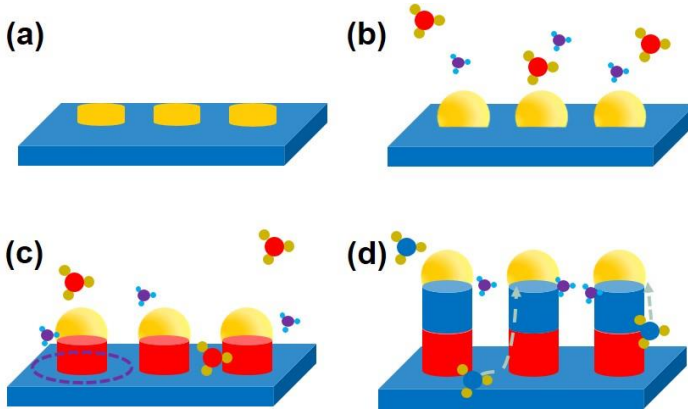


**Figure 4.** A schematic of the VLS growth of nanowires. (a) The substrate with gold particles patterned on its top. (b) The supply of III-V precursors which alloy with the gold particles. (c) The particle gets super-saturated, and III-V materials start precipitating and crystallizing underneath the particle. (d) With the changes of the precursor supply, heterostructures are formed in the nanowires.

A typical growth experiment of our samples consists of the following steps: The temperature of the reactor is ramped to 280 °C when TMIn and $PH_3$ are supplied. With the incorporation of In into the gold (Au) particle, the Au particle turns into Au-In alloy. This low-temperature nucleation step helps to preserve the seed particle pattern during the following high-temperature annealing at 550 °C when particle moving and merging can happen [58]. After the low-temperature nucleation step, the reactor temperature is raised to 550 °C for the desorption of surface oxide on the substrate. Then, the reactor temperature was set at 440 °C for InP/GaInP nanowire growth. When the

nanowire growth is completed, the group III supply is switched off. The heater is switched off at the same time. The reactor is cooled down with a group V overpressure, with the aim to prevent material decomposition because of the high volatility of phosphorous atoms.

### 3.1.2 Formation of nanowire heterostructures

One of the main challenges of nanowire growth is the formation of heterostructures [64][65]. After the switch-on of the material supply for the heterointerface, the composition of the seed particle is changed, i.e. the chemical potential is changed. This will lead to a change in the contact angle between the particle and the nanowire. Consequently, the diameter and the crystal structure can be changed. Moreover, nanowire kinking can happen due to the change of surface energy during the heterostructure growth, which means a change in nanowire growth direction, especially for ternary nanowire growth [66]. For example, GaP segment can be grown vertically on InP bottom segment in <111>B direction, but the reverse case (InP grown on top of GaP) is not as easy. It usually ends up with kinked nanowires [67]. In the proposal of the GaInP/InP double junction nanowire solar cell, a GaInP top cell needs to be grown on top of an InP bottom cell. As a result of the switch-on of TMGa for GaInP segment growth, the chemical potential and surface energy of the seed particle is changed, followed by nanowire diameter change and possibly nanowire kinking.

Besides kinked nanowires, we also observed inhomogeneous growth rate for GaInP nanowires during the growth of either GaInP nanowires on InP substrates or a GaInP segment on top of the InP segment. As shown in Figure 5, the ultra-long nanowires stand out from the other normal wires and have a smaller diameter (See the inset of Figure 5). We found that when there is more TMGa supplied, there are more ultra-long wires. In the transmission electron microscopy (TEM) measurement on the ultra-long nanowires, we observed that the ultra-long nanowires always contain diagonal twin planes in them. More in-depth understanding of the origin of this phenomenon is needed. As an attempt to eliminate such inhomogeneity, alternative Ga precursor, i.e. triethylgallium (TEG) has been studied for the growth of GaInP nanowires by which the number of ultra-long nanowires was greatly reduced [Paper X].
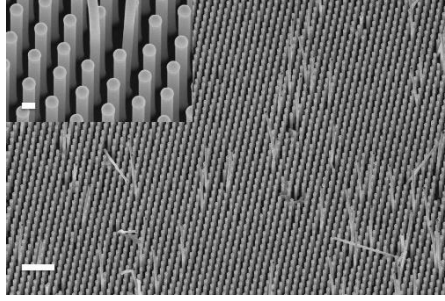
**Figure 5.** A $Ga_{0.3}In_{0.7}P$ nanowire sample with kinked and ultra-long nanowires. The scale bar is 2 µm. The inset has a scale bar of 200 nm.

Another challenge in forming heterostructures is the control of the heterojunction sharpness in terms of material and doping transition. On the one hand, the nanowires grown in a MOVPE system can be influenced by the reactor memory effect and the particle reservoir effect due to the VLS growth mechanism. One consequence of such effects is that the growth sequence of two materials can affect the sharpness of the heterointerfaces [68]. On the other hand, the introduction of dopants which can affect the chemical potential of the seed particle can further complicate the scenario [Paper III].

The reactor memory effect and the particle reservoir effect make the growth interface change not as abrupt as the input gas change resulting in a carry-over of adatoms for the following-grown materials. Specifically, it can be either that the newly-introduced species diffuse on the surfaces (reactor sidewalls, susceptor surface, substrate surface) before reaching the nanowire growth front, or the newly-switched-off gases are desorbed slowly from the susceptor and/or the reactor sidewalls, thus remaining in the reactor for a period of time. A typical case for the reactor memory effect is the magnesium (Mg) doping in gallium nitride (GaN) growth [69]. For species with high vapor pressure and low solubility in the gold particle, such as phosphorous (P) and sulfur (S), the reactor memory effect is considered less prominent because they can be quickly desorbed [70]. For those species with low vapor pressure, such as Mg and antimony (Sb) [71], they will remain in the reactor for much longer time. Consider the formation of the InP:Sn/GaInP:Zn tunnel junction, there will be a zinc (Zn) concentration saturation delay for reaching the degenerate doping level needed at the heterointerface. Hence, the delay will result in a gradual *p*-type doping profile which is unfavorable for carrier tunneling [Paper III].

The particle reservoir effect is another factor that will smear out the heterojunction sharpness. Since many adatoms incorporate into the nanowire via the seed particle, the materials stored in the particle will not be desorbed immediately after the switch-off of the gas supply. The stored materials will

14

gradually precipitate from the seed particle. For example, the particle reservoir effect brings dual influence to the growth of the InP:Sn/GaInP:Zn (i.e. *n*-InP/*p*-GaInP) tunnel diode. One is regard to the doping. Since Sn has a relatively large solubility in the particle [72], there is some amount of Sn remaining in the seed particle after the Sn precursor is switched off. The remained Sn will gradually precipitate into the following *p*-type GaInP segment, resulting in a compensation to the *p* doping which is undesired. The other influence is that because of a higher affinity of In in the Au particle than that of Ga [68][73][74][75], a sharper InGaP (bottom)/InP (top) heterointerface than the InP (bottom)/GaInP (top) heterointerface can be achieved.

### 3.1.3 In situ surface treatment

During the nanowire growth, axial growth is usually accompanied by radial growth, due to the mass transportation along the nanowire sidewalls and the limited diffusion length of adatoms. Any radial growth is not preferred in the formation of axial *p-i-n* junctions because it can short-circuit the junction. In previous studies, hydrogen chloride (HCl) and hydrogen bromide (HBr) have been introduced in situ to remove any radial growth for InP [76] and GaP [77] nanowires, respectively. The radial growth was successfully suppressed, but the use of hydrogen halides can bring additional effects to the nanowires, such as nanowire surface and defect incorporation. Considering the large surface-to-volume ratio of nanowires, this can be important for the optoelectronic properties of nanowires. In our study, we found that the optimal HCl flow used for InP nanowire growth which completely removes the radial growth also leads to the longest carrier lifetime in photoluminescence measurements [Manuscript XII].

Since the surface of III - V materials is an important factor for the optoelectronic properties, many studies have been reported on surface passivation for both planar materials [78] and nanomaterials [79][80]. The usual solutions for nanowire surface passivation include chemical treatment [81], in situ growth of a heterogeneous shell [82] and ex situ deposition of protective capping layers [83][84]. In situ passivation is expected to achieve a better passivation effect than the ex situ passivation. This is because the nanowire surface is preserved without being exposed outside the growth environment in the in situ passivation. For an ideal shell, it is supposed to prevent carriers from recombining at the nanowire surface. Therefore, it should have a higher bandgap than that of the nanowire core, forming a sufficient barrier at the conduction band and valence band surrounding the core. Then, a sufficient thickness of the shell is necessary to prevent any carriers from

tunneling to the outer surface of the shell and recombining. Lastly, a relatively high quality of the shell is needed. Any recombination center introduced by the shell is undesired, such as oxides and lattice-mismatch related defects.

To passivate the GaInP nanowires, we have designed the shell parameters and developed the growth of an aluminium indium phosphide (AlInP) shell to the GaInP nanowires [Manuscript VI]. The optical measurements show that the photoluminescence carrier lifetime is improved from approximately 200 ps to 1.5 ns, which is comparable to the best passivated GaAs nanowires [78].

## 3.2 Nanowire processing

To contact a single nanowire for electrical measurements, one approach is to measure the nanowire as grown, i.e. by using a nanoprobe to contact the nanowire tip as the top contact and using the backside of the substrate as a back contact. The other approach is to break the nanowires from the substrates, transfer them to an insulating substrate, define and deposit metal contact on the lying-down nanowires. In the first approach, any nanoprobe with the ability to inject a current through the tip can be used, such as a conductive atomic force microscopy (cAFM) [85], or an electron beam induced current (EBIC) system equipped with nanoprobes [86][87]. Compared to the first approach, the second approach has the advantage of a larger contact area, which facilitates Ohmic contact formation. However, there are still challenges in forming Ohmic contacts to $p$-type InP and GaInP nanowires, due to the Fermi level pinning, where surface states tend to pin the Fermi level at a certain position at the nanowire surface [28][88][89].

In this thesis, three types of samples were processed into single nanowire devices: the doped GaInP nanowires for doping evaluation, the InP/GaInP nanowire tunnel diodes and the $n$-$pin$ structure samples (See Chapter 4.3.1). The contact design and processing procedure are similar, and the differences lie in the specific $n$- or $p$-type contact material deposited to the specific ends of the nanowire. For $p$-(Ga)InP, Ti/Zn/Au is used. For $n$-(Ga)InP, Ti/Au is used. The detailed processing procedure can be found in Paper I, II, and III. A processed GaInP nanowire for doping evaluation is shown in Figure 7 in Chapter 3.3.2.

# 3.3 Nanowire characterization

## 3.3.1 Material characterization

After the growth, the nanowires are usually inspected by scanning electron microscopy (SEM) which is a powerful tool to image the nanowire morphology with information on nanowire diameter, length, orientation and preliminary indication on the crystal structure. In a SEM system, an incident electron beam can be generated by either a thermionic filament which is heated by a filament current for electron generation or a field emission gun (FEG) where the electrons are pulled off the cold filament by a strong electrostatic field. Then, the electrons are accelerated by an electromagnetic field. The electron beam is then focused and scanned on the sample. When the incident electrons interact with the sample, electrons scatter either elastically or inelastically which creates an excitation volume where various types of products can be generated, including auger electrons, secondary electrons, backscattered electrons, and characteristic X-rays. The imaging system of a SEM can detect the ejection of secondary electrons and/or the backscattered electrons.

X-ray diffraction (XRD), with its non-destructive and rapid feedback, is widely used for material composition analysis. The composition homogeneity both across the sample and along an individual nanowire´s axis is an important issue for nanowires [90]. A $\omega$ - $2\theta$ scan is normally performed with a sweep from the $2\theta$ angle of InP to that of GaP. The peak position, width, and shape of the $\omega$ - $2\theta$ curve indicate the material composition and its distribution.

To inspect the crystal structure and chemical composition of nanowires, transmission electron microscopy (TEM) equipped with energy dispersive X-ray spectroscopy (EDX, EDS or XEDS) is used. Compared to SEM, TEM makes use of the transmitted electrons instead of the scattered ones. Therefore, it utilizes a much higher energy electron beam and requires the sample to be sufficiently thin (For a 300 kV electron gun, the specimen should not be thicker than a scale of ~100 nm). By tilting the sample holder, the inspected nanowire is aligned to the incident electron beam with the {1-10} facets being perpendicular to the electron beam so that the atomic column of the (111)A and (111)B facets is lying parallel to the beam. Hence, the contrast from crystal structure is maximized. High-resolution TEM images can be taken for the analysis of the crystal structure. By converging the electron beam to a small and incoherent probe, the beam can be scanned across the sample. This Scanning TEM (STEM) mode can be used for imaging, meanwhile, it is also beneficial for high spatial resolution chemical composition analysis. X-rays are generated from a small illuminated volume of the sample by the scanning beam. When

an incoming electron scatters inelastically, the specimen ejects a core electron from the inner shell. The excited atom may relax by allowing an electron from an outer shell to fill the empty state in the inner shell. Consequently, an X-ray photon is emitted with the characteristic energy of the excited element which can be detected and identified. The standardless quantitative analysis is used for the determination of chemical composition. For most elements, the typical detectable limit is approximately 0.5 – 1 at. %.

Photoluminescence characterization is a convenient method which requires no prior processing to assess the optical quality of materials. The photoluminescence is the light emission from materials after the absorption of photons during which electrons transit from low energy states to high energy states. When a semiconductor material is excited by photons with energy larger than the semiconductor bandgap, electrons in the valence band can be excited to the conduction band. Correspondingly, holes are generated simultaneously at the valence band. Then, the excess electrons and holes can recombine radiatively through the bandgap or via the local states in the bandgap. In either way, photons with characteristic energy will be emitted. The characteristic emission of photons reflects the electronic structure, material composition, crystal quality and the competition between radiative and non-radiative recombination. A sketch of the photocarrier generation and recombination processes is illustrated in Figure 6. The carrier concentration for highly doped nanowires can be extracted by the method of fitting the high energy tail of the PL spectrum which corresponds to the extent of band filling effect due to the high doping level [91]. We found that the carrier concentration of *n*-type GaInP nanowires calculated from the PL spectrum has a good agreement with that obtained from the Hall-effect measurement [Paper II].
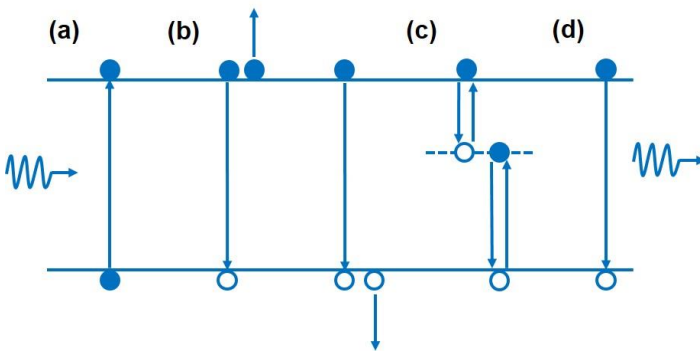


**Figure 6.** Schematic of the generation and recombination of photocarriers. (a) Electrons are excited by photon absorption. (b) Auger recombination (nonradiative). (c) Shockley-Read-Hall recombination (nonradiative). (d) Radiative recombination with photon emission.

For the application of GaInP nanowires in optoelectronic devices, it is essential to understand the recombination and photoconductivity dynamics of photo-generated charge carriers. In Paper V, we did a comprehensive study by measuring the photoluminescence carrier lifetime, photoconductivity and photocarrier mobility of GaInP nanowires with different Ga composition. Time-resolved photoinduced luminescence (TRPL) measurement was used for the study of the charge recombination dynamics. The TRPL decay under different excitation photon flux can reveal if the recombination of photogenerated carriers is bimolecular dominated or Auger-recombination dominated. Time-resolved THz spectroscopy (TRTS) was used for the analysis of the mobility dynamics and carrier recombination process. In contrast to PL, TRTS generates an excitation which initiates a change in far-infrared absorption properties on a sub-picosecond timescale. It is selectively sensitive to photoconductivity which is a product of the mobility and concentration of photocarriers. The fs-transient absorption (TA) can measure the changes in the absorbance/transmittance of the sample. The absorbance at a particular wavelength was measured as a function of time after excitation by a flash of light. The overall charge recombination via both radiative and nonradiative channels can be resolved in the TA decay kinetics. By combing all these measurements, we found that the fast hole- and electron-trapping rates and the nonradiative recombination rate are all strongly dependent on Ga composition in the GaInP nanowires, in agreement with the expected formation of deep traps under increased Ga composition [Paper V].

### 3.3.2 Device characterization

The I-V measurement on single contacted nanowires is performed at a CASCADE probe station operated at room temperature. It is equipped with four tungsten probes and a Keithley 4200 semiconductor characterization system. For the nanowire tunnel diode samples, the I-V curves were measured. For the *n-pin* structure samples, I-V curves both in dark and under illumination were measured. The devices were illuminated by a 532-nm laser. In the doping evaluation studies on GaInP nanowires, for the four-probe resistivity measurements, voltage sweep was done between the two end contacts of the nanowire, and the resulting current was measured. The voltage at the different positions along the device was measured, and the electrical resistance of each segment was calculated by dividing the voltage drop between each contact pair by the current. For the backgated field-effect transistor (FET) measurement, two probes were connected to the bondpads as source and drain, respectively. The backside of the device substrate was used for back gate voltage sweeping. A detailed description of the measuring methods can be found in

Paper II. The SEM image of a processed single nanowire device is shown in Figure 7.
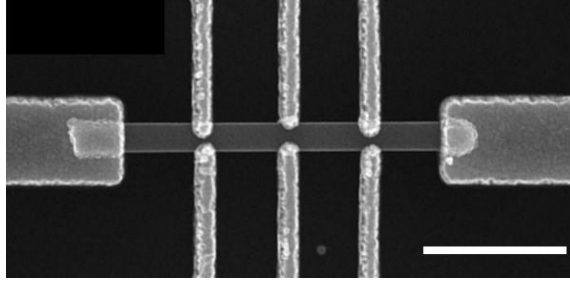


**Figure 7.** A processed single nanowire device with contact pairs for the four-probe resistivity, backgated FET, and Hall-effect measurements. The scale bar is 1 μm.

The method for the extraction of carrier concentrations from the four-probe and backgated FET measurements is described as follows:

In the Drude model, conductivity (σ) is defined as:

$$\sigma = nq\mu \qquad (3.1)$$

where σ is the conductivity, n is the carrier concentration, q is the elementary charge, and μ is the carrier mobility. According to Equation 3.1, the conductivity and carrier mobility is needed for the calculation of the carrier concentration.

The conductivity can be obtained from the four-probe I-V measurement. The mobility can be extracted from the backgated FET measurement. By sweeping the back-gate voltage, the conducting channel is modulated and the transconductance can be extracted from Equation 3.2:

$$g_m = \frac{dI_{SD}}{dV_G}\Big|_{V_{SD}=constant} = \frac{C\mu}{L^2}V_{SD} \qquad (3.2)$$

where $g_m$ is the transconductance, $I_{SD}$ is the source-drain current, $V_G$ is the gate voltage, C is the capacitance of the nanowire, and L is the length of the active region. Once the $g_m$ and C is known, the mobility μ can be extracted.

Here, C is estimated as a metallic cylinder surrounded by a layer of dielectric, and is expressed as:

$$C = \frac{2\pi L \varepsilon_0 \varepsilon_r}{\cosh^{-1}(\frac{R+h}{R})} \qquad (3.3)$$

Where $\varepsilon_0$ is the vacuum permittivity, $\varepsilon_r$ is the relative dielectric constant, R is the nanowire radius, and h is the distance between the gate and the bottom of

the nanowire [92]. Note that in our devices, the dielectric area used for calculation only covers approximately half of the nanowire surface because of the presence of the lifting layer which partially buries the lying-down nanowire [93]. Therefore, C should be divided by 2 here.

Through the method described above, the carrier concentration can be calculated. However, the accuracy of this approach is limited [94][95], due to the deviation of the estimation of the transconductance which is virtually gate-voltage-dependent, the estimation of the capacitance and the ignorance of the influence of surface states on carrier concentration distribution [96]. As an alternative method to avoid such inaccuracy, Hall-effect measurement was carried out for the doping evaluation studies [Paper II].

In the Hall-effect measurement, the magnetic field applied vertically to the current flow will lead to a so-called Hall voltage due to the Lorentz force. The Hall-effect measurement is widely used in conventional planar characterization as an effective method to determine the carrier concentration in doped samples. The Hall-effect measurement has been enabled on nanowires not until the recent years [97][98]. The challenge in performing Hall-effect measurements on nanowires is the limited surface area for the formation of the high-quality electrical contact. In our studies, three pairs of Hall contacts are deposited for investigating the spatial distribution of carrier concentrations. The related device fabrication requires a precise control of contact definition by electron beam lithography (EBL), metal evaporation and lift-off.

In addition to the electrical measurement by contacting lying-down nanowires, electron beam induced current measurement (EBIC) can provide further information on the depletion region and minority carrier diffusion length [86]. Under the illumination of the electron beam, the nanowire absorbs the energy of the incident electrons. Consequently, excess minority carriers are generated and then separated by the built-in field of the *pn*-junction. When scanning the electron beam on the sample, the EBIC signal and profile can reveal the location and characteristics of the *pn*-junction. EBIC measurements on the as-grown nanowire samples were performed with the help of a nanoprobe-system from Kleindiek Nanotechnik, mounted inside a Hitachi SU8010 SEM. The samples were cleaved so that one can access nanowires in the center of the sample in a cross-section view. The substrate was glued to an SEM stub by use of silver paste, and a tungsten nanoprobe was put in direct contact with the seed particle on the tip of the nanowire for back and front contacts respectively.

# 4. Steps towards InP/GaInP tandem junction solar cells

In this chapter, we will move step by step from the research of binary nanowires towards more complex binary-and-ternary-combined nanowires. Starting from the successful InP nanowire solar cell device [99], the first step forward is the synthesis and doping control of the GaInP nanowires, which is the building block of the upper cell of the proposed tandem junction solar cell design [33]. Compared to the binary InP nanowire growth, the ternary GaInP nanowires involve more challenges in the control of the nanowire length uniformity, the composition homogeneity, and the dopant incorporation. Once we have achieved a high yield of GaInP nanowires with desired doping level, we can form a GaInP *p-i-n* junction and characterize it. Meanwhile, as a critical component connecting subcells in the tandem junction solar cell, InP/GaInP tunnel diodes need to be established. When we have realized all the components of the double junction solar cell (i.e. the two subcells and the tunnel junction), the ensemble of the tandem junction solar cell becomes possible. To reduce the complexity for characterizing the final device with multiple junctions, we designed and fabricated an intermediate test structure, which consists of the tunnel junction and the upper cell, enabling the diagnostic of the components' performance. These studies will lay the foundation for the realization of a nanowire tandem junction solar cell.

## 4.1 Doping evaluation of *n*- and *p*-type GaInP nanowires

We did a systematic study on the growth and doping evaluation of *p*- and *n*-type GaInP nanowires by using different dopant species, which are reported in [Paper I] and [Paper II], respectively.

### 4.1.1 *n*-type doping

S, selenium (Se), silicon (Si), tin (Sn), and tellurium (Te), are the commonly-used *n*-type dopants for the planar InP-GaInP material system [54]. As discussed in Chapter 3, since the dopants can affect the VLS growth mechanism of nanowires, this becomes an important issue to consider when choosing proper dopant species for nanowires. In our studies, hydrogen sulfide ($H_2S$) and tetraethyltin (TESn) were tested for GaInP nanowires as they had been successively applied in the doping of InP nanowires [100].

On the one hand, S mainly incorporates into the GaInP nanowire via the vapor-solid boundary due to its high vapor pressure and low solubility in Au particle. This makes it incorporate/desorb immediately after $H_2S$ is switched on/off, respectively. Therefore, a sharp doping profile can be expected. The similar atom size of S and P favors S to be a substitutional dopant of P, hence a high doping level is expected. However, S has a prominent effect on the crystal structure of GaInP nanowires. It is believed that S lowers the surface energy of the seed particle and enlarges the wetting angle [101]. As a result, WZ crystal structure is favored and the nanowire diameter increases [102][103]. Additionally, S is also known as a surface passivator [102]. It changes the surface diffusion length of adatoms, especially for those with a relatively small surface diffusion length, e.g. In. This can result in a more uniform composition distribution along the nanowire axis [Paper II].

On the other hand, Sn has a relatively large solubility in Au particle. It does not have a prominent influence on the crystal structure and nanowire diameter of GaInP nanowires. The stability of Sn favors its use in nanowire devices. However, the large solubility brings a large particle reservoir effect, which means that a sharp high Sn doping profile is difficult to achieve. In the doping evaluation study, we observed a carrier concentration saturation by using TESn as dopant precursor at approximately $3 \times 10^{18}$ cm$^{-3}$. By contrast, the highest S doped GaInP nanowire sample reaches a carrier concentration of $1 \times 10^{19}$ cm$^{-3}$ [Paper II]. The difference in the maximum doping levels between the two dopant species is probably because of the different incorporation pathways and different segregation coefficients of Sn and S [104][105].

### 4.1.2 *p*-type doping

The typical *p*-type dopant species for planar GaInP are Mg and Zn [54]. bis-cyclopentadienyl magnesium ($Cp_2Mg$) is the commonly-used precursor for Mg doping with a relatively high vapor pressure and strong reactor memory effect [54]. In our study, $Cp_2Mg$ was investigated for *p*-type doping of GaInP

nanowires. A series of samples with varying Cp₂Mg molar fractions from low to high were grown. Increasing the amount of Cp₂Mg supply to a high level resulted in an inhomogeneous length of GaInP nanowires, as shown in Figure 8.
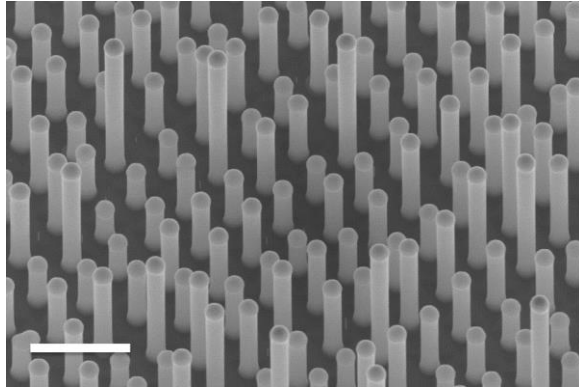


**Figure 8.** GaInP nanowires grown with high Cp₂Mg flows. The scale bar is 1 μm.

The electrical measurement of the Mg doped GaInP nanowire samples showed no observable effective doping. This was unexpected, considering the successful doping in planar GaInP growth by using Cp₂Mg which reaches a carrier concentration of $10^{18}$ cm$^{-3}$ [106]. One possibility is that the Mg incorporation is low in our GaInP nanowires, as it has been found that the Mg incorporation decreases rapidly with growth temperature in the Mg doped planar GaInP grown by CBE [106]. Another possibility is that the Mg dopants incorporated successfully into the nanowires but were not activated. Therefore, as an attempt to activate the possibly incorporated Mg dopants, a rapid thermal annealing step was performed on the processed devices at 350 °C, for 10 s, and in the forming gas. However, we did not observe any change in the I-V measurements. In conclusion, our results show that Cp₂Mg is not an effective dopant precursor for GaInP nanowires grown in VLS mechanism.

By contrast, Zn doping shows effective *p*-type doping. However, the use of diethylzinc (DEZn) facilitates Ga incorporation due to the enhanced pyrolysis of TMGa in the presence of the ethyl radicals from the decomposed DEZn. It also changes the wetting angle of the seed particle, introducing ZB crystal structure with twin planes in GaInP nanowires [Paper I]. Due to the limited diffusion length of In adatoms, the amount of In adatoms reaching the nanowire growth front decreases with the growth of the nanowires. To balance the decreasing In adatoms and obtain a constant Ga composition, the GaInP composition homogeneity along the nanowire can be achieved by gradually decreasing the TMGa supply [107]. Even though *p*-type behavior has been

observed in the backgated FET measurements of Zn doped GaInP nanowires, it was not possible to accurately extract the carrier concentration from the four probe and the backgated FET measurements due to the highly resistive Schottky contacts to the *p*-GaInP nanowires. Hence, the Zn doping level was difficult to assess by the electrical measurements on single nanowire devices. Despite the poor contacts, degenerate *p*-type doping has been confirmed by the realization of *n*-InP/*p*-GaInP nanowire tunnel diodes [Paper I].

A recent study on X-ray fluorescence (XPF) measurements of the Zn doped GaInP nanowires revealed a carrier concentration of $10^{19}$ cm$^{-3}$ in our most highly doped *p*-GaInP nanowires [Manuscript XIII]. However, the maximum doping level was reached after about 700-nm growth of the nanowires in our system.

# 4.2 InP/GaInP nanowire tunnel diodes

If we consider several *pn*-junctions to be connected in series with the intention to form a tandem junction solar cell, a back-to-back *pn*-junction would be formed in the opposite direction between the two adjacent *pn*-junctions. Assume this reverse *pn*-junction was a normal diode, then the carriers would have to overcome a large barrier of the reverse *pn*-junction when the other *pn*-junctions are forward biased. Therefore, a normal back-to-back *pn*-junction would cause large photovoltage loss in a tandem junction solar cell. To minimize the photovoltage loss, a tunnel diode is needed between the two subcells, through which carriers can tunnel through the *pn*-junction barrier instead of having to overcome the *pn*-junction barrier.

Invented by Leo Esaki in 1958 [108], planar tunnel diodes have been extensively investigated with applications in electronic and optoelectronic devices such as tunneling static random access memory (SRAM), tunnel FETs, and solar cells. A tunnel diode is a *pn*-junction with degenerate doping at both *p*- and *n*-sides where the Fermi level enters the conduction band of the *n*-side and the valence band of the *p*-side. Because of the degenerate doping at the heterojunction, the depletion region is narrow with a favorable distance for carrier tunneling. The amount of degeneracy of doping in tunnel diodes is typically 50 - 200 meV [109]. Due to the lack of knowledge and difficulties in nanowire growth and doping of nanowires, nanowire tunnel diodes have only been demonstrated in unitary and binary materials [30][110][111][112][113] [114][115]. However, nanowire tunnel diodes with material combinations optimal for solar energy harvesting (usually involve ternaries) have not been reported until the study in [Paper III].
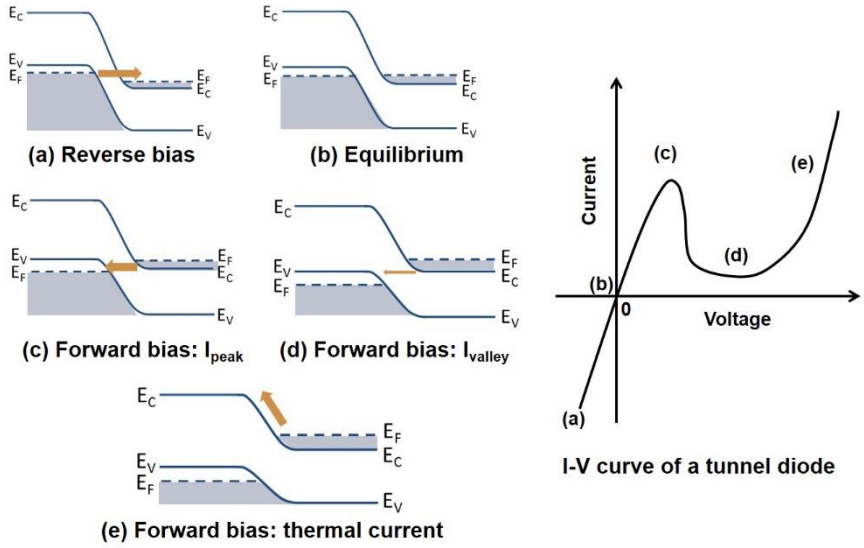
**Figure 9.** Schematic of a typical I-V curve of a tunnel diode (right) with band diagrams at the corresponding voltage bias (left). Left: Band diagrams of a tunnel diode under various voltage bias. (a) Reverse bias, Zener tunneling. (b) Equilibrium, zero net current. (c) Forward bias, I=$I_{peak}$. (d) Forward bias, I=$I_{valley}$. (e) Forward bias, diffusion of thermal electrons. Right: The typical I-V curve of a tunnel diode.

The principles of a tunnel diode are shown in Figure 9. When in reverse bias (Fig. 9a), the quasi-Fermi level at the $p$-side rises compared to that at the $n$-side, i.e. there is a band of occupied energy states at the $p$-side and unoccupied energy states at the $n$-side. Therefore, a direct Zener tunneling from the $p$-side to the $n$-side will occur. When in equilibrium (Fig. 9b), a uniform Fermi level is achieved across the $pn$-junction, hence there is no net current. When in forward bias (Fig. 9c), the quasi-Fermi level at the $n$-side rises compared to that at the $p$-side. There are a band of occupied energy states at the $n$-side and a band of unoccupied energy states at the $p$-side. Thus, electrons can tunnel from the $n$-side to the $p$-side. When the bias increases to the peak voltage $V_P$, the tunneling current reaches its peak value $I_P$. When the forward bias further increases (i.e. for $V_P < V < V_V$, where $V_V$ is the valley voltage) (Fig. 9d), the number of unoccupied states at the $p$-side decreases so the tunneling current decreases. With the further increase of the bias voltage (i.e. for $V > V_V$), there are no unoccupied states at the $p$-side because of the bandgap. Therefore, the tunneling current can no longer flow. Instead, when the forward bias increases further (Fig. 9e), a thermal current will flow.

To design a tunnel junction for tandem junction solar cells, there are several requirements to fulfill. First, degenerate doping is a prerequisite for direct tunneling. To have a high tunneling probability, the depletion region of the junction should be sufficiently thin to enable carrier tunneling. The direct

27

tunneling current $T_t$ is exponentially dependent on the effective barrier thickness as described in Equation (4.1) [109]:

$$T_t \approx \exp(\frac{-4\sqrt{2m^*}E_g^{3/2}}{3q\hbar\varepsilon})\exp(\frac{-E_\perp\pi\sqrt{2m^*E_g}}{q\hbar\varepsilon}) \qquad (4.1)$$

where $E_g$ is the bandgap energy, $E_\perp$ is the transverse energy of electron associated with momentum perpendicular to the direction of tunneling, q is the elementary charge, ℏ is the reduced Plank constant, $m^*$ is the effective mass, and ε is the built-in electric field of the junction. The equation implies that the less abrupt the heterojunction, the weaker the built-in electric field, and thus the smaller the tunneling current. Therefore, a sharp material transition and doping profile at the heterojunction is necessary. Second, in order to minimize the electrical and optical loss, the electrical resistivity of the tunnel diode should be as small as possible, and the entire tunnel junction should be as thin as possible [116]. Third, the peak current of the tunnel junction should be larger than the expected photocurrent of the device. Otherwise, the tunnel junction could work in an unstable status, which could lead to a large voltage drop over the tunnel junction [117].

In the formation of InP/GaInP nanowire tunnel diodes, several challenges are involved for a sharp transition of material and doping, as discussed in Chapter 3.1.2. To establish a tunnel diode used for the InP/GaInP nanowire double junction solar cell, we designed a set of samples as illustrated in Figure 10. The configurations were designed in either the forward *n*-InP/*p*-GaInP direction or the reverse *p*-GaInP/*n*-InP direction. Different dopant species were tested for the *n*-InP segments, based on their different capabilities as discussed in Paper II. Through our investigation, the InP:Sn/GaInP:Zn configuration and the GaInP:Zn/InP:S configuration were found working as tunnel diodes [Paper III].
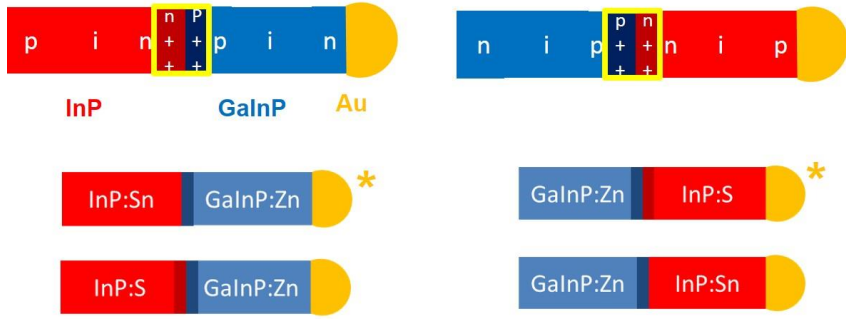
**Figure 10.** Schematic of the design of tandem structures and the corresponding tunnel junction configurations. Left: The forward tandem structure (top) and the corresponding tunnel junction configurations (bottom). Right: The reverse tandem structure (top) and the corresponding tunnel junction configurations (bottom). Star marks indicate the working tunnel diodes achieved in our study.

To analyze the reasons for the non-working configurations, one working configuration and one non-working configuration were measured by EBIC measurement. The non-working configuration showed a wider depletion region than the working configuration, indicating a lower doping level which reduced the tunneling probability. A recent study by electron holography performed in a TEM equipment also supports a wider depletion region for the non-working devices [Manuscript XIV]. According to the peak current density, the peak-to-valley-current (PVCR) ratio, and the electrical resistivity measured in our working tunnel diodes, they are eligible to be applied in an InP/GaInP tandem junction solar cell.

We have measured the working tunnel diode sample (GaInP:Zn/InP:S configuration) by contacting the as-grown nanowire by a nanoprobe installed in a SEM system. It is known that, during the cooling-down process of the nanowire growth, the particle reservoir effect can lead to a small extra nanowire segment ("neck") grown on top of the nanowire. Together with the fact that $H_2S$ desorbs rapidly from the growth front after the supply is switched off, this may result in a low $n$-doped InP "neck" left on top of the nanowire, which can worsen the contact between the nanowire and the nanoprobe of the EBIC setup. To investigate whether such a low $n$-doped InP "neck" degraded the contact properties or not, we switched the $n$-type dopant species from S to Sn for the InP segment after the growth of the heterojunction (i.e. We grew a GaInP:Zn/InP:S/InP:Sn configuration). Compared with the GaInP:Zn/InP:S configuration, we found an improvement of the peak current and the PVCR of the tunnel diode [Paper IV].

# 4.3 Build up InP/GaInP double junction solar cells

The realization of InP/GaInP nanowire tunnel diodes is a milestone towards the InP/GaInP double junction solar cell (DJSC). However, the property of a simple tunnel diode could be different from that grown in a more complex structure. For example, the shortened length of the tunnel junction in a combination with other *pn*-junctions could be insufficient for reaching the degenerate doping owing to the reactor memory effect and/or particle reservoir effect as discussed in Chapter 3.1.2. Since the I-V characteristics of the ultimate DJSC structure can be complicated to interpret, it is of importance to design an intermediate structure as a transition from single-junction solar cell to double-junction solar cells for diagnostics and optimization.

## 4.3.1 Intermediate test structure

The intermediate test structure (short for "*n-pin*") consisting of a working *n*-InP/*p*-GaInP tunnel junction and a GaInP *p-i-n* junction was designed. The schematic of the *n-pin* structure is shown in Figure 11. With this structure, we can conveniently form Ohmic contacts on both *n*-InP and *n*-GaInP end segments. The *n*-InP was designed to 1 µm so that the tunnel junction and the upper GaInP cell can be grown at the same position as they were designed in the DJSC structure.
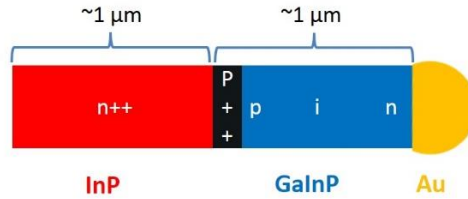


**Figure 11.** Schematic of the *n-pin* structure.

For comparison, a *p*-InP/GaInP *p-i-n* structure, namely "*p-pin*" structure was grown. By the I-V measurement in the EBIC setup, we found that the nominally intrinsic GaInP segment was *p*-type in the *p-pin* structure, however, it was *n*-type in the *n-pin* structure. This was evidenced by the location of the EBIC signal. As shown in Figure 12, the depletion region is located at the nominal *n*-GaInP/*i*-GaInP interface in the *p-pin* structure (Fig. 12b). By contrast, the depletion region is located at the nominal *i*-GaInP/*p*-GaInP interface in the *n-pin* structure (Fig. 12d). These results indicate memory

effects from dopants used in the firstly-grown *n*- or *p*-InP segment, similar with the observations in [118]. Considering the growth of the full tandem structure, we can anticipate that multiple memory effects may occur for different junctions, bringing challenges in the growth of the desired structure. Solutions for the multiple memory effects can be compensating doping and/or growth interruption.
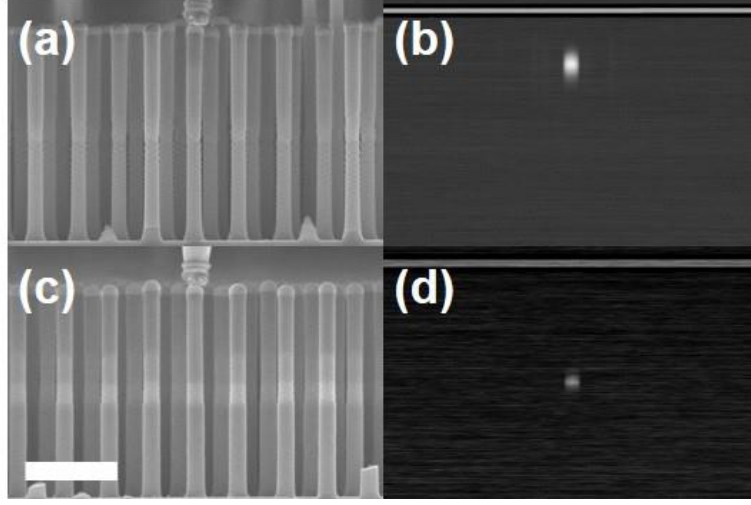


**Figure 12.** EBIC measurements on the *p-pin* and *n-pin* structures. (a) SEM image of the *p-pin* structure with 50-nm-*p++* GaInP segment. (b) The EBIC signal of the *p-pin* structure. (c) SEM image of the *n-pin* structure with 50-nm-*p++* GaInP segment. (d) The EBIC signal of the *n-pin* structure. The scale bar is 1 µm.

To investigate the influence of the *p++* segment length on the performance of the *n-pin* structures, we grew a series of *n-pin* samples with a variation of the *p++* segment length (approximately 30 nm, 50 nm, and 90 nm, respectively). Single nanowire devices were processed and measured. In the I-V measurements under illumination, a 512-nm laser was used. The results were shown in Figure 13.
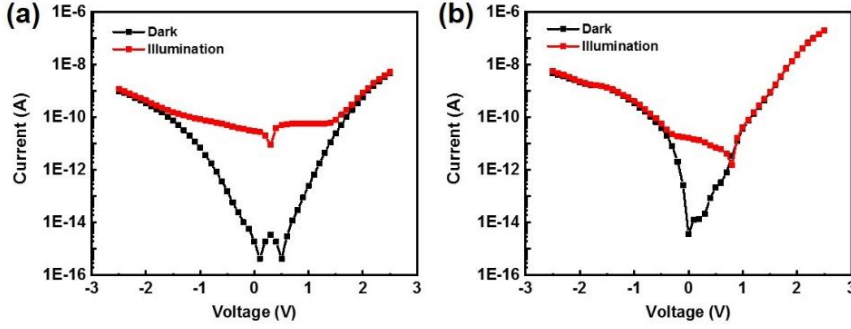
**Figure 13.** I-V measurements in dark and under illumination of the *n-pin* structures with varied *p++* segment length. (a) The sample with 30-nm-*p++* segment. (b) The sample with 50-nm-*p++* segment.

In the I-V curve under illumination of the sample with 30-nm-*p++* segment (Figure 13a), we observed a positive current plateau at the positive bias which reduces the "$V_{oc}$" of the device (i.e. the voltage at the crossover of the I-V curve with the X-axis) to ~0.3 V, compared to that of ~0.95 V for a *p-pin* structure. By contrast, as shown in Figure 13b, we observed the absence of the positive current plateau in the samples with 50-nm-*p++* segment, and so as the sample with 90-nm-*p++* segment (not shown). The mechanism behind this phenomenon is not fully understood yet. However, we speculate that in the sample with the 30-nm-*p++* segment, it could be insufficiently long to reach degenerate *p*-doping for the GaInP segment due to the saturation delay of Zn concentration. Therefore, the tunnel junction could work not as it should, but as a reversely-connected *pn*-junction. Under illumination, it could contribute a positive photovoltage and photocurrent, in the opposite direction to that of the GaInP *p-i-n* junction. These results indicate that a sufficiently long *p++* segment is needed for the tunnel junction working in the complex structures. We are working on a more detailed analysis, and a manuscript is under preparation [Manuscript VII].

The next step forward will be to optimize the growth and performance of the tunnel diodes, the performance of individual subcells, the growth of the tandem structure, and the current matching between the two subcells. Additionally, to enable the use of the reverse tandem structure (as shown in Figure 10) which may have an advantage of a better tunnel junction (i.e. the *p*-GaInP/*n*-InP tunnel junction shows a higher peak current and PVCR than the *n*-InP/*p*-GaInP tunnel junction. See [Paper III] ), the reverse devices will need to be turned upside down eventually to have a higher bandgap subcell on top. Therefore, the development of the peel-off of nanowires is necessary. We have developed an effective peel-off technique for transferring nanowires from

the native substrate to a foreign substrate, which will be discussed in the next chapter.

# 5. Nanowire peel-off

The cost of conventional planar III-V devices includes a large portion of the expensive substrates. The substrates usually have a thickness in the order of hundreds of micrometers, which is much thicker than the epitaxial layers which are usually only a few micrometers. Transferring the epitaxial layers and reusing the substrate for growth can greatly reduce the cost, thus releasing the potential of III-V devices for large-scale applications. The lift-off technology has been investigated for various thin film devices [19][119]. For nanowire arrays which only cover a small portion of the substrate surface, it is promising to peel them off from the homogeneous substrate [120]. In this thesis, we have developed a technology to peel the dense nanowire array by embedding them into a polymer.

## 5.1 Peel-off and processing

Previous studies on the peel-off technique have been reported for nanowires with a relatively large length (typically >5 μm), small diameter and small density [121][122][123][124]. The transfer of nanowires is effective, but not many of the peeled films have been processed into a device [125][126]. When it comes to our samples which are shorter (~ 2 μm in length), thinner (~ 200 nm in diameter) and denser (500 nm in pitch) than the reported ones, the reported methods did not work on our samples. Thus, the peel-off becomes more challenging.

To successfully peel off the nanowire array, the desired polymer should have good penetration to the bottom of nanowires, proper adhesion to the nanowires and the substrate surface, and sufficient robustness to withstand the mechanical peeling process. Considering the requirements for optical measurements and the compatibility to the following solar cell processing steps, the polymer is also required to be transparent to visible light and easy to remove after peel-off, respectively. After testing several other chemicals including polydimethylsiloxane (PDMS) and perylene, we found the "First Contact" (FC) polymer an optimal option. The FC polymer is a product of the Photonic

Cleaning Technologies LLC [127]. The colorless FC that we use is an optically-transparent, inert, and plastic film. Its main application is the surface cleaning of optics.

The specifics of the peeling procedure are described as follows: First, cover the sample surface with the FC solvent by using a pippet. After the deposition, the solvent begins to cure in the air. Normally, several layers of FC are added. This is to make sure a sufficient robustness to endure the peeling process. A sufficient cure of the polymer lasts for approximately 48 hours. Then, the peeling starts with the revealing of a corner of the sample. The peeling of the polymer film is done by use of a tweezer, as illustrated in Figure 14. In order to improve the uniformity of the force applied to the polymer film, a razor can be applied. Another way is to embed a plastic mesh in between the several FC layers, which can help to avoid too much stretch in the film during the peeling. The use of a roller for the peeling can also be helpful [128][129].
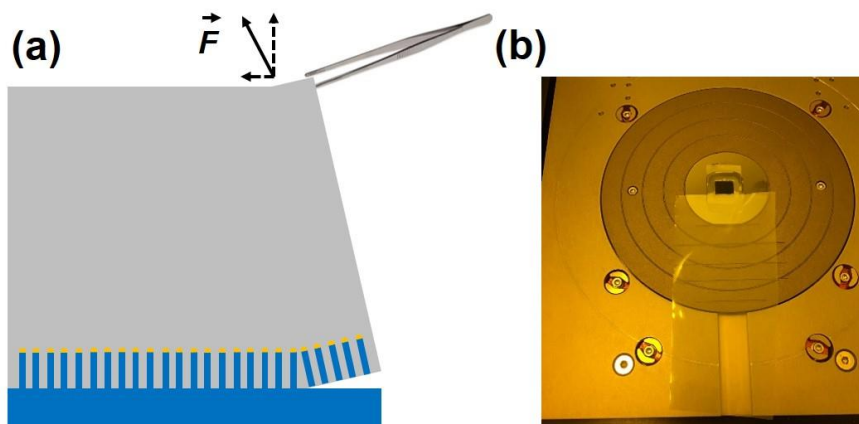


**Figure 14.** Schematic of the peeling procedure of the polymer film with nanowires embedded. (a) The pulling of the film by using a tweezer. (b) The use of a plastic mesh and the attachment of a tape to the polymer film is to have a more uniform peeling force.

A peeled-off film is shown in Figure 15. The dark color indicates a good embedding of the nanowire arrays in the film and the preservation of the array order which maintains the light trapping advantage.
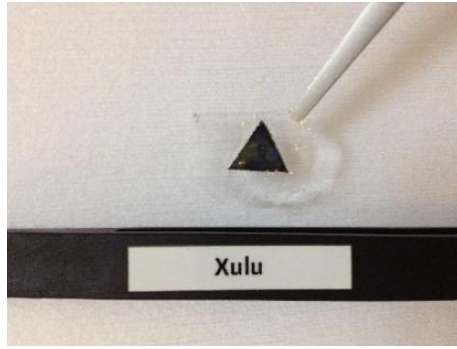
**Figure 15.** A peeled-off FC film with nanowires embedded in the triangular area.

As shown in Figure 16a, the substrate after peel-off shows that most of the nanowires were broken from the nanowire bottom, and only a few nanowires and stubs were left on the substrate. The SEM image (Figure 16b) was also taken from the backside of the polymer film, which evidenced that the order of the nanowire array was basically preserved. However, it was hard to judge if the nanowires were tilted in the film due to the minor unflatness of the film and how it was placed on the SEM holder. This peeling approach turned out to be effective and has been applied to the samples involved in Paper V, VIII, IX, and XII.
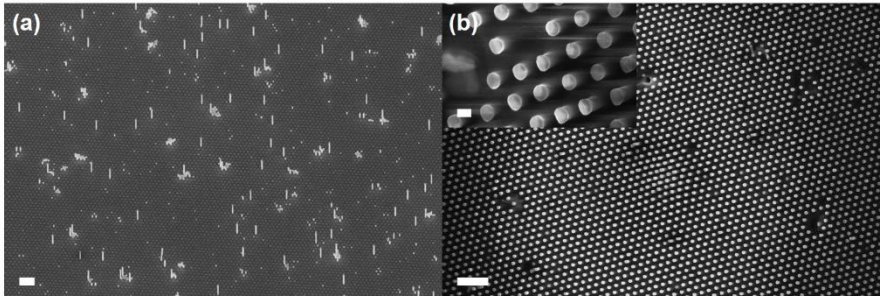


**Figure 16.** SEM images of a peeled-off sample. (a) The substrate after peel-off. The scale bar is 2 μm. The image is taken at 30° tilt. (b) The backside of the polymer film. The scale bar is 2 μm. The inset has a scale bar of 200 nm. The images are taken at 0° tilt.

To process the peeled polymer film into a device, the necessary step is to reveal the nanowire bottom and tip for the deposition of back and front contacts, respectively. The nanowire bottom was revealed by reactive ion etching (RIE) by approximately 200 - 300 nm. A layer of contact materials either (Ti/Au) or indium tin oxide (ITO) was deposited. The contact metal embeds part of the nanowire bottom to help to keep the nanowires standing after the removal of the polymer. Since the FC film has a thickness of several hundreds of

micrometers, dry etching of the film by using reactive ion etching (RIE) is not allowed in the cleanroom at NanoLund according to the concern on the contamination of the chamber. Alternatively, it is possible to dissolve the FC film in a dedicated solution named the "thinner". Note that the dissolution of a crosslinked polymer will not be complete, and the swelling of the film during the dissolution process is inevitable which can affect the nanowire orientation. The schematic of the peel-off and the processing procedure is shown in Figure 17.
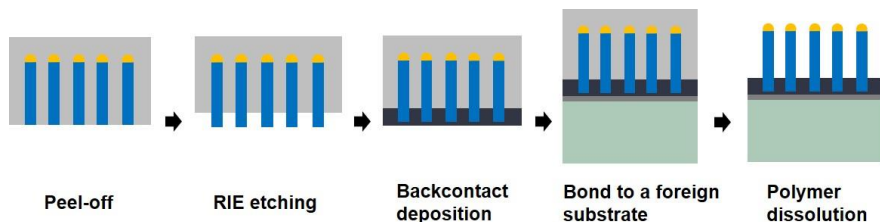


**Figure 17.** The peel-off and the related processing procedure.

The dissolution of the film in the thinner takes approximately 36 hours. After that, the peeled film was put on a foreign substrate, for instance, a Si substrate or a copper coin. However, the nanowires were found tilted after the dissolution of FC polymer, as shown in Figure 18a. The tilt is undesired, as it brings a shading effect to the adjacent nanowires, thus affecting the device performance. The origin of the tilt can be tracked to the stretch of the film during the peeling process, the insufficient support from the back contact metal, and/or the unstable dissolution process. Regarding the unstable dissolution process, a solution can be to use the critical point dryer to reduce the surface tension during the dissolution of FC polymer. Additionally, the thin layer of nanowires with the backcontact material was found with cracks after polymer dissolution which is undesired for device fabrication, as shown in Figure 18b. These issues remain as challenges for further development.
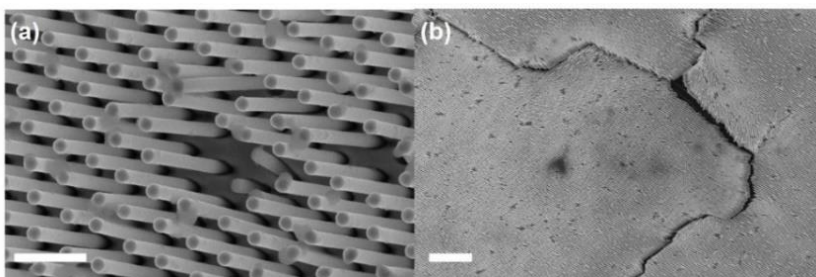


**Figure 18.** SEM images of a peeled sample after polymer dissolution. (a) Top view of the sample, 0° tilt. The scale bar is 1 μm. (b) Top view of an area with cracks, 0° tilt. The scale bar is 10 μm.

# 6. Summary and outlook

With the studies presented in this thesis, we investigated the topics necessary for the development of the InP/GaInP nanowire tandem junction solar cell, including:

(1) The growth of doped GaInP nanowires and doping evaluation of both $n$-type and $p$-type GaInP nanowires were investigated. A wide range of $n$-type and $p$-type doping levels can be achieved suitable for the use in the tandem junction solar cells.

(2) InP/GaInP nanowire tunnel diodes were established. This is a milestone towards the InP/GaInP double junction nanowire solar cell. Different dopant species and growth directions were studied. We observed a wider depletion region for the non-working devices which was the result of a gradual transition of materials and doping. The reproductivity and homogeneity of the tunnel diodes will need further optimization.

(3) We combined the working tunnel junction with the GaInP upper cell as an intermediate test structure to the full tandem structure. We found that the memory effects from the firstly-grown segment will unintentionally dope the nominal $i$-segment of the upper cell, affecting the property of the GaInP upper cell. This knowledge indicates that multiple memory effects can be involved in the growth of the tandem junction solar cell, for which a solution will be needed.

(4) As an attempt to peel off the nanowires and be able to use the inverted-grown reverse tandem structure, the peel-off technique has been developed. The embedding of nanowires in the polymer is effective. However, the tilt of nanowires and cracks of the backcontact material after the removal of the polymer constitute issues to be further improved.

In summary, these studies have laid the foundation for the realization of a nanowire tandem junction solar cell. The future developments will involve the demonstration of a tandem junction solar cell indicated by $V_{oc}$ addition, growth optimization to solve the unintentional doping, current matching between subcells, and the development of the peel-off technique and the related processing which can lead to a flexible device.

# 7. References

[1]     "The Paris agreement." [Online]. Available: https://unfccc.int/
        process/the-paris-agreement/the-paris-agreement.

[2]     International Energy Agency, "Key world energy statistics 2017,"
        2017.    [Online].    Available:    http://www.iea.org/publications/
        freepublications/publication/KeyWorld2017.pdf.

[3]     A. Luque and S. Hegedus, *Handbook of photovoltaic science and
        engineering*. John Wiley & Sons, Ltd, 2011.

[4]     M. M. May, H.-J. Lewerenz, D. Lackner, F. Dimroth, and T.
        Hannappel, "Efficient direct solar-to-hydrogen conversion by in situ
        interface transformation of a tandem structure," *Nat. Commun.*, vol.
        6, no. 1, p. 8286, 2015.

[5]     C. Liu, N. P. Dasgupta, and P. Yang, "Semiconductor nanowires for
        artificial photosynthesis," *Chem. Mater.*, vol. 26, no. 1, pp. 415–422,
        2014.

[6]     K. G. T. Hollands and M. F. Lightstone, "A review of low-flow,
        stratified-tank solar water heating systems," *Sol. Energy*, vol. 43, no.
        2, pp. 97–105, 1989.

[7]     D. Mills, "Advances in solar thermal electricity technology," *Sol.
        Energy*, vol. 76, no. 1–3, pp. 19–31, 2004.

[8]     J. Nelson, *The physics of solar cells*. Imperial College Press, 2003.

[9]     A. Jaeger-Valdau, "PV status report 2017," 2017. [Online].
        Available: http://publications.jrc.ec.europa.eu/repository/bitstream/
        JRC108105/kjna28817enn.pdf.

[10]    International Energy Agency, "World energy resources," 2016.
        [Online].        Available:        https://www.iea.org/publications/
        freepublications/publication/KeyWorld2016.pdf.

[11]    World Energy Council, "World energy scenarios: composing energy
        futures    to    2050,"    2013.    [Online].    Available:    https://
        www.worldenergy.org/wp-content/uploads/2013/09/World-Energy
        -Scenarios_Composing-energy-futures-to-2050_Full-report. pdf.

[12]    "Photovoltaics report," 2018. [Online]. Available: https://www.ise.

fraunhofer.de/content/dam/ise/de/documents/publications/studies/P
hotovoltaics-Report.pdf.

[13]   M. A. Green, Y. Hishikawa, E. D. Dunlop, D. H. Levi, J. Hohl-
Ebinger, and A. W. Y. Ho-Baillie, "Solar cell efficiency tables
(version 51)," *Prog. Photovoltaics Res. Appl.*, vol. 26, no. 1, pp. 3–
12, 2018.

[14]   A. Blakers, N. Zin, K. R. McIntosh, and K. Fong, "High efficiency
silicon solar cells," *Energy Procedia*, vol. 33, pp. 1–10, 2013.

[15]   "Efficiency chart." [Online]. Available: https://www.nrel.gov/pv/
assets/images/efficiency-chart.png.

[16]   F. Dimroth, "High-efficiency solar cells from III-V compound
semiconductors," *Phys. Status Solidi C Conf.*, vol. 3, no. 3, pp. 373–
379, 2006.

[17]   M. T. Borgström *et al.*, "Towards nanowire tandem junction solar
cells on silicon," *IEEE J. Photovoltaics*, vol. 8, no. 3, pp. 733–740,
2018.

[18]   A. Beien, C. Löpez, A. M. Vega, and A. L. Löpez, *Next generation
of photovoltaics new concepts*. Springer, 2012.

[19]   P. Demeester, I. Pollentier, P. De Dobbelaere, C. Brys, and P. Van
Daele, "Epitaxial lift-off and its applications," *Semicond. Sci.
Technol.*, vol. 8, no. 6, p. 1124, 1993.

[20]   J. De Boeck and G. Borghs, "III–V on Si: heteroepitaxy versus lift-
off techniques," *J. Cryst. Growth*, vol. 127, no. 1–4, pp. 85–92,
1993.

[21]   M. S. Gudiksen, L. J. Lauhon, J. Wang, D. C. Smith, and C. M.
Lieber, "Growth of nanowire superlattice structures for nanoscale
photonics and electronics," *Nature*, vol. 415, no. 6872, pp. 617–620,
2002.

[22]   L. Samuelson *et al.*, "Semiconductor nanowires for novel one-
dimensional devices," *Phys. E Low-dimensional Syst.
Nanostructures*, vol. 21, no. 2–4, pp. 560–567, 2004.

[23]   M. Heurlin *et al.*, "Continuous gas-phase synthesis of nanowires
with tunable properties," *Nature*, vol. 492, no. 7427, pp. 90–94,
2012.

[24]   N. Anttu and H. Q. Xu, "Coupling of light into nanowire arrays and
subsequent absorption," *J. Nanosci. Nanotechnol.*, vol. 10, no. 11,
pp. 7183–7187, 2010.

[25]   D. Van Dam *et al.*, "High efficiency nanowire solar cells with
omnidirectionally enhanced absorption due to self-aligned indium-

tin-oxide mie scatterers," *ACS Nano*, vol. 10, no. 12, pp. 11414–11419, 2016.

[26]    R. R. Lapierre *et al.*, "III-V nanowire photovoltaics: review of design for high efficiency," *Phys. Status Solidi - Rapid Res. Lett.*, vol. 7, no. 10, pp. 815–830, 2013.

[27]    G. Otnes and M. T. Borgström, "Towards high efficiency nanowire solar cells," *Nano Today*, vol. 12, pp. 31–45, 2017.

[28]    M. T. Borgström *et al.*, "Nanowires with promise for photovoltaics," *IEEE J. Sel. Top. Quantum Electron.*, vol. 17, no. 4, pp. 1050–1061, 2011.

[29]    H. J. Joyce *et al.*, "III–V semiconductor nanowires for optoelectronic device applications," *Prog. Quantum Electron.*, vol. 35, no. 2–3, pp. 23–75, 2011.

[30]    M. Heurlin *et al.*, "Axial InP nanowire tandem junction grown on a silicon substrate," *Nano Lett.*, vol. 11, no. 5, pp. 2028–2031, 2011.

[31]    T. J. Kempa, B. Tian, D. R. Kim, J. Hu, X. Zheng, and C. M. Lieber, "Single and tandem axial *p-i-n* nanowire photovoltaic devices," *Nano Lett.*, vol. 8, no. 10, pp. 3456–3460, 2008.

[32]    M. Yao *et al.*, "Tandem solar cells using GaAs nanowires on Si: design, fabrication, and observation of voltage addition," *Nano Lett.*, vol. 15, no. 11, pp. 7217–7224, 2015.

[33]    Y. Chen, M.-E. Pistol, and N. Anttu, "Design for strong absorption in a nanowire array tandem solar cell," *Sci. Rep.*, vol. 6, no. 1, p. 32349, 2016.

[34]    K. J. Bachmann, "Properties, preparation, and device applications of Indium Phosphide," *Annu. Rev. Mater. Sci.*, vol. 11, no. 1, pp. 441–484, 1981.

[35]    S. Adachi, "Optical properties of $In_{(1-x)}Ga_xAs_yP_{(1-y)}$ alloys," *Phys. Rev. B*, vol. 39, no. 17, pp. 12612–12621, 1989.

[36]    A. Mishra *et al.*, "Polarization and temperature dependence of photoluminescence from zincblende and wurtzite InP nanowires," *Appl. Phys. Lett.*, vol. 91, no. 26, p. 263104, 2007.

[37]    J. W. Nicklas and J. W. Wilkins, "Accurate ab initio predictions of III–V direct-indirect band gap crossovers," *Appl. Phys. Lett.*, vol. 97, no. 9, p. 91902, 2010.

[38]    I. Vurgaftman, J. R. Meyer, and L. R. Ram-Mohan, "Band parameters for III-V compound semiconductors and their alloys," *J. Appl. Phys.*, vol. 89, no. 11, pp. 5815–5875, 2001.

[39]  A. Onton, M. R. Lorenz, and W. Reuter, "Electronic structure and luminescence processes in In$_{1-x}$Ga$_x$P alloys," *J. Appl. Phys.*, vol. 42, no. 9, pp. 251103–41118, 1971.

[40]  A. Bensaada *et al.*, "Band alignment in Ga$_x$In$_{1-x}$P/InP heterostructures," *Appl. Phys. Lett.*, vol. 64, no. 3, pp. 273–275, 1994.

[41]  "PICS3D user's manual," 1995. [Online]. Available: http://citeseerx.ist.psu.edu/viewdoc/download?doi=10.1.1.31.920&rep=rep1&type=pdf.

[42]  S. Assali *et al.*, "Direct band gap wurtzite gallium phosphide nanowires," *Nano Lett.*, vol. 13, no. 4, pp. 1559–1563, 2013.

[43]  A. Berg *et al.*, "Growth and characterization of wurtzite GaP nanowires with control over axial and radial growth by use of HCl in situ etching," *J. Cryst. Growth*, vol. 386. pp. 47–51, 2014.

[44]  F. Bechstedt and A. Belabbes, "Structure, energetics, and electronic states of III–V compound polytypes," *J. Phys. Condens. Matter*, vol. 25, no. 27, p. 273201, 2013.

[45]  A. Belabbes, C. Panse, J. Furthmüller, and F. Bechstedt, "Electronic bands of III-V semiconductor polytypes and their alignment," *Phys. Rev. B*, vol. 86, no. 7, p. 75208, 2012.

[46]  A. De and C. E. Pryor, "Predicted band structures of III-V semiconductors in the wurtzite phase," *Phys. Rev. B*, vol. 81, no. 15, p. 155210, 2010.

[47]  A. I. Persson, M. W. Larsson, S. Stenström, B. J. Ohlsson, L. Samuelson, and L. R. Wallenberg, "Solid-phase diffusion mechanism for GaAs nanowire growth," *Nat. Mater.*, vol. 3, no. 10, pp. 677–681, 2004.

[48]  M. de la Mata *et al.*, "A review of MBE grown 0D, 1D and 2D quantum structures in a nanowire," *J. Mater. Chem. C*, vol. 1, no. 28, p. 4300, 2013.

[49]  K. Hiruma *et al.*, "GaAs free-standing quantum-size wires," *J. Appl. Phys.*, vol. 74, no. 5, pp. 3162–3171, 1993.

[50]  H. Pan *et al.*, "Growth of Si nanowires by thermal evaporation," *Nanotechnology*, vol. 16, no. 4, pp. 417–421, 2005.

[51]  X. Duan and C. M. Lieber, "Laser-assisted catalytic growth of single crystal GaN nanowires," *J. Am. Chem. Soc.*, vol. 122, no. 1, pp. 188–189, 2000.

[52]  N. Kornienko, D. D. Whitmore, Y. Yu, S. R. Leone, and P. Yang, "Solution phase synthesis of indium gallium phosphide alloy

nanowires," *ACS Nano*, vol. 9, no. 4, pp. 3951–3960, 2015.

[53] E. Barrigón *et al.*, "GaAs nanowire *pn*-junctions produced by low-cost and high-throughput aerotaxy," *Nano Lett.*, vol. 18, no. 2, pp. 1088–1092, 2018.

[54] G. B. Stringfellow, *Organometallic vapor-phase epitaxy: theory and practice*. Elsevier Science, 1989.

[55] J. Johansson, B. A. Wacaser, K. A. Dick, and W. Seifert, "Growth related aspects of epitaxial nanowires," *Nanotechnology*, vol. 17, no. 11, pp. S355–S361, 2006.

[56] A. Berg, F. Lenrick, N. Vainorius, J. P. Beech, L. R. Wallenberg, and M. T. Borgström, "Growth parameter design for homogeneous material composition in ternary $Ga_xIn_{1-x}P$ nanowires," *Nanotechnology*, vol. 26, no. 43, p. 435601, 2015.

[57] K. A. Dick, "A review of nanowire growth promoted by alloys and non-alloying elements with emphasis on Au-assisted III-V nanowires," *Prog. Cryst. Growth Charact. Mater.*, vol. 54, no. 3–4, pp. 138–173, 2008.

[58] G. Otnes *et al.*, "Strategies to obtain pattern fidelity in nanowire growth from large-area surfaces patterned using nanoimprint lithography," *Nano Res.*, vol. 10, no. 2, p. 729, 2017.

[59] L. C. Campos *et al.*, "Vapor-solid-solid growth mechanism driven by epitaxial match between solid AuZn alloy catalyst particles and ZnO nanowires at low temperatures," *Adv. Mater.*, vol. 20, no. 8, pp. 1499–1504, 2008.

[60] S. Kodambaka, J. Tersoff, M. C. Reuter, and F. M. Ross, "Germanium nanowire growth below the eutectic temperature," *Science*, vol. 316, no. 5825, pp. 729–732, 2007.

[61] P. Caroff, J. Bolinsson, and J. Johansson, "Crystal phases in III-V nanowires: from random toward engineered polytypism," *IEEE J. Sel. Top. Quantum Electron.*, vol. 17, no. 4, pp. 829–846, 2011.

[62] N. Akopian, G. Patriarche, L. Liu, J.-C. Harmand, and V. Zwiller, "Crystal phase quantum dots," *Nano Lett.*, vol. 10, no. 4, pp. 1198–1201, 2010.

[63] K. A. Dick, C. Thelander, L. Samuelson, and P. Caroff, "Crystal phase engineering in single InAs nanowires," *Nano Lett.*, vol. 10, no. 9, pp. 3494–3499, 2010.

[64] J. Johansson and K. A. Dick, "Recent advances in semiconductor nanowire heterostructures," *CrystEngComm*, vol. 13, no. 24, p. 7175, 2011.

[65] J. K. Hyun, S. Zhang, and L. J. Lauhon, "Nanowire heterostructures," *Annu. Rev. Mater. Res.*, vol. 43, no. 1, pp. 451–479, 2013.

[66] V. G. Dubrovskii, "Understanding the vapor–liquid–solid growth and composition of ternary III–V nanowires and nanowire heterostructures," *J. Phys. D. Appl. Phys.*, vol. 50, no. 45, p. 453001, 2017.

[67] K. A. Dick *et al.*, "The morphology of axial and branched nanowire heterostructures," *Nano Lett.*, vol. 7, no. 6, pp. 1817–1822, 2007.

[68] K. A. Dick, J. Bolinsson, B. M. Borg, and J. Johansson, "Controlling the abruptness of axial heterojunctions in III-V nanowires: beyond the reservoir effect," *Nano Lett.*, vol. 12, no. 6, pp. 3200–3206, 2012.

[69] Y. Ohba and A. Hatano, "A study on strong memory effects for Mg doping in GaN metalorganic chemical vapor deposition," *J. Cryst. Growth*, vol. 145, no. 1–4, pp. 214–218, 1994.

[70] M. T. Borgström, M. A. Verheijen, G. Immink, T. De Smet, and E. P. A. M. Bakkers, "Interface study on heterostructured GaP-GaAs nanowires," *Nanotechnology*, vol. 17, no. 16. pp. 4010–4013, 2006.

[71] M. Ek *et al.*, "Formation of the axial heterojunction in GaSb/InAs(Sb) nanowires with high crystal quality," *Cryst. Growth Des.*, vol. 11, no. 10, pp. 4588–4593, 2011.

[72] J. Ciulik and M. R. Notis, "The Au-Sn phase diagram," *J. Alloys Compd.*, vol. 191, pp. 71–78, 1993.

[73] P. Krogstrup *et al.*, "Junctions in axial III - V heterostructure nanowires obtained via an interchange of group III elements," *Nano Lett.*, vol. 9, no. 11, pp. 3689–3693, 2009.

[74] M. Paladugu *et al.*, "Nature of heterointerfaces in GaAs/InAs and InAs/GaAs axial nanowire heterostructures," *Appl. Phys. Lett.*, vol. 93, no. 10, p. 101911, 2008.

[75] S. G. Ghalamestani, M. Ek, and K. A. Dick, "Realization of single and double axial InSb-GaSb heterostructure nanowires," *Phys. status solidi - Rapid Res. Lett.*, vol. 8, no. 3, pp. 269–273, 2014.

[76] M. T. Borgström *et al.*, "In situ etching for total control over axial and radial nanowire growth," *Nano Res.*, vol. 3, no. 4, pp. 264–270, 2010.

[77] A. Berg, K. Mergenthaler, M. Ek, M. E. Pistol, L. R. Wallenberg, and M. T. Borgström, "In situ etching for control over axial and radial III-V nanowire growth rates using HBr," *Nanotechnology*, vol. 25, no. 50, p. 505601, 2014.

[78]   L. G. Meiners and H. H. Wieder, "Semiconductor surface passivation," *Mater. Sci. Reports*, vol. 3, no. 3–4, pp. 139–216, 1988.

[79]   Y. Dan, K. Seo, K. Takei, J. H. Meza, A. Javey, and K. B. Crozier, "Dramatic reduction of surface recombination by in situ surface passivation of Silicon nanowires," *Nano Lett.*, vol. 11, no. 6, pp. 2527–2532, 2011.

[80]   H. Hasegawa and M. Akazawa, "Surface passivation technology for III–V semiconductor nanoelectronics," *Appl. Surf. Sci.*, vol. 255, no. 3, pp. 628–632, 2008.

[81]   M. H. Sun, H. J. Joyce, Q. Gao, H. H. Tan, C. Jagadish, and C. Z. Ning, "Removal of surface states and recovery of band-edge emission in InAs nanowires through surface passivation," *Nano Lett.*, vol. 12, no. 7, pp. 3378–3384, 2012.

[82]   J. W. W. van Tilburg, R. E. Algra, W. G. G. Immink, M. Verheijen, E. P. A. M. Bakkers, and L. P. Kouwenhoven, "Surface passivated InAs/InP core/shell nanowires," *Semicond. Sci. Technol.*, vol. 25, no. 2, p. 24011, 2010.

[83]   V. Dhaka *et al.*, "Protective capping and surface passivation of III-V nanowires by atomic layer deposition," *AIP Adv.*, vol. 6, p. 15016, 2016.

[84]   L. E. Black, A. Cavalli, M. A. Verheijen, J. E. M. Haverkort, E. P. A. M. Bakkers, and W. M. M. Kessels, "Effective surface passivation of InP nanowires by atomic-layer-deposited $Al_2O_3$ with POx interlayer," *Nano Lett.*, vol. 17, no. 10, pp. 6287–6294, 2017.

[85]   Z. Fan *et al.*, "Electrical and photoconductive properties of vertical ZnO nanowires in high density arrays," *Appl. Phys. Lett.*, vol. 89, no. 21, p. 213110, 2006.

[86]   I. Åberg *et al.*, "A GaAs nanowire array solar cell with 15.3% efficiency at 1 sun," *IEEE J. Photovoltaics*, vol. 6, no. 1, pp. 185–190, 2016.

[87]   K. Arstila *et al.*, "Nanoprober-based EBIC measurements for nanowire transistor structures," *Microelectron. Eng.*, vol. 105, pp. 99–102, 2013.

[88]   T. Haggren *et al.*, "InP nanowire *p*-type doping via zinc indiffusion," *J. Cryst. Growth*, vol. 451, pp. 18–26, 2016.

[89]   M. H. M. van Weert *et al.*, "Large redshift in photoluminescence of *p*-doped InP nanowires induced by Fermi-level pinning," *Appl. Phys. Lett.*, vol. 88, no. 4, p. 43109, 2006.

[90]  D. Kriegner *et al.*, "Structural investigation of GaInP nanowires using X-ray diffraction," *Thin Solid Films*, vol. 543. pp. 100–105, 2013.

[91]  D. Lindgren *et al.*, "Study of carrier concentration in single InP nanowires by luminescence and Hall measurements," *Nanotechnology*, vol. 26, p. 45705, 2015.

[92]  J. Wallentin and M. T. Borgström, "Doping of semiconductor nanowires," *J. Mater. Res.*, vol. 26, no. 17, pp. 2142–2156, 2011.

[93]  O. Hultin, G. Otnes, M. T. Borgström, M. Björk, L. Samuelson, and K. Storm, "Comparing Hall effect and field effect measurements on the same single nanowire," *Nano Lett.*, vol. 16, no. 1, pp. 205–211, 2016.

[94]  O. Wunnicke, "Gate capacitance of back-gated nanowire field-effect transistors," *Appl. Phys. Lett.*, vol. 89, no. 8, p. 83102, 2006.

[95]  D. R. Khanal and J. Wu, "Gate coupling and charge distribution in nanowire field effect transistors," *Nano Lett.*, vol. 7, no. 9, pp. 2778–2783, 2007.

[96]  X. Jiang, Q. Xiong, S. Nam, F. Qian, Y. Li, and C. M. Lieber, "InAs/InP radial nanowire heterostructures as high electron mobility devices," *Nano Lett.*, vol. 7, no. 10, pp. 3214–3218, 2007.

[97]  K. Storm *et al.*, "Spatially resolved Hall effect measurement in a single semiconductor nanowire," *Nat. Nanotechnol.*, vol. 7, no. 11, pp. 718–722, 2012.

[98]  C. Blömers *et al.*, "Hall effect measurements on InAs nanowires," *Appl. Phys. Lett.*, vol. 101, no. 15, p. 152106, 2012.

[99]  J. Wallentin *et al.*, "InP nanowire array solar cells achieving 13.8% efficiency by exceeding the ray optics limit," *Science*, vol. 339, no. 6123, pp. 1057–1060, 2013.

[100] F. Lindelöw *et al.*, "Doping evaluation of InP nanowires for tandem junction solar cells," *Nanotechnology*, vol. 27, no. 6, 2016.

[101] J. Wallentin *et al.*, "Probing the wurtzite conduction band structure using state filling in highly doped InP nanowires," *Nano Lett.*, vol. 11, no. 6, pp. 2286–2290, 2011.

[102] F. Glas, J. C. Harmand, and G. Patriarche, "Why does wurtzite form in nanowires of III-V zinc blende semiconductors?," *Phys. Rev. Lett.*, vol. 99, no. 14, pp. 3–6, 2007.

[103] V. G. Dubrovskii, N. V. Sibirev, J. C. Harmand, and F. Glas, "Growth kinetics and crystal structure of semiconductor nanowires," *Phys. Rev. B*, vol. 78, no. 23, p. 235301, 2008.

[104] A. Royle, B. W. Straughan, P. J. Tufton, and E. W. Williams, "Crystal growth and properties of group IV doped indium phosphide," *J. Cryst. Growth*, vol. 13–14, pp. 640–646, 1972.

[105] O. Oda, *Compound semiconductor bulk materials and characterizations*, vol. 10, no. 9. World Scientific Publishing Co. Pte. Ltd., 2007.

[106] S. Courmont, P. Maurel, C. Grattepain, and J. C. Garcia, "Mg doping of GaInP grown by chemical beam epitaxy using bis-cyclopentadienyl magnesium," *Appl. Phys. Lett.*, vol. 64, no. 11, pp. 1371–1373, 1994.

[107] A. Berg, F. Lenrick, N. Vainorius, J. P. Beech, L. R. Wallenberg, and M. T. Borgström, "Growth parameter design for homogeneous material composition in ternary $Ga_xIn_{1-x}P$ nanowires," *Nanotechnology*, vol. 26, no. 43, p. 435601, 2015.

[108] L. Esaki, "New phenomenon in narrow germanium *p-n* junctions," *Phys. Rev.*, vol. 109, no. 2, pp. 603–604, 1958.

[109] S. M. Sze and K. K. Ng, *Physics of semiconductor devices*. Wiley-Interscience, 2007.

[110] J. Wallentin, J. M. Persson, J. B. Wagner, L. Samuelson, K. Deppert, and M. T. Borgström, "High-performance single nanowire tunnel diodes," *Nano Lett.*, vol. 10, no. 3, pp. 974–979, 2010.

[111] B. M. Borg, K. A. Dick, B. Ganjipour, M.-E. Pistol, L.-E. Wernersson, and C. Thelander, "InAs/GaSb heterostructure nanowires for tunnel field-effect transistors," *Nano Lett.*, vol. 10, no. 10, pp. 4080–4085, 2010.

[112] H. Schmid, C. Bessire, M. T. Björk, A. Schenk, and H. Riel, "Silicon nanowire Esaki diodes," *Nano Lett.*, vol. 12, no. 2, pp. 699–703, 2012.

[113] B. Ganjipour *et al.*, "High current density Esaki tunnel diodes based on GaSb-InAsSb," *Nano Lett.*, vol. 11, pp. 4222–4226, 2011.

[114] W. Y. Fung, L. Chen, and W. Lu, "Esaki tunnel diodes based on vertical Si-Ge nanowire heterojunctions," *Appl. Phys. Lett.*, vol. 99, no. 9, pp. 20–22, 2011.

[115] S. Nadar, C. Rolland, J. F. Lampin, X. Wallart, P. Caroff, and R. Leturcq, "Tunnel junctions in a III–V nanowire by surface engineering," *Nano Res.*, vol. 8, no. 3, pp. 980–989, 2015.

[116] I. García, I. Rey-Stolle, and C. Algora, "Performance analysis of AlGaAs/GaAs tunnel junctions for ultra-high concentration photovoltaics," *J. Phys. D. Appl. Phys.*, vol. 45, no. 4, p. 45101,

2012.

[117] W. Guter and A. W. Bett, "IV-characterization of devices consisting of solar cells and tunnel diodes," *Conf. Rec. 2006 IEEE 4th World Conf. Photovolt. Energy Conversion, WCPEC-4*, vol. 1, pp. 749–752, 2007.

[118] G. Otnes *et al.*, "Understanding InP nanowire array solar cell performance by nanoprobe-enabled single nanowire measurements," *Nano Lett.*, DOI: 10.1021/acs.nanolett.8b00494, 2018.

[119] C. W. Cheng, K. T. Shiu, N. Li, S. J. Han, L. Shi, and D. K. Sadana, "Epitaxial lift-off process for gallium arsenide substrate reuse and flexible electronics," *Nat. Commun.*, vol. 4, p. 1577, 2013.

[120] A. Zhang, G. Zheng, and C. M. Lieber, *Nanowires*. Springer, 2016.

[121] K. E. Plass *et al.*, "Flexible polymer-embedded Si wire arrays," *Adv. Mater.*, vol. 21, no. 3, pp. 325–328, 2009.

[122] S. Chattopadhyay, Y. F. Huang, Y. J. Jen, A. Ganguly, K. H. Chen, and L. C. Chen, "Anti-reflecting and photonic nanostructures," *Mater. Sci. Eng. R.*, vol. 69, no. 1–3, pp. 1–35, 2010.

[123] S. L. Diedenhofen, O. T. A. Janssen, G. Grzela, E. P. A. M. Bakkers, and J. Gómez Rivas, "Strong geometrical dependence of the absorption of light in arrays of semiconductor nanowires," *ACS Nano*, vol. 5, no. 3, pp. 2316–2323, 2011.

[124] A. J. Standing, S. Assali, J. E. M. Haverkort, and E. P. A. M. Bakkers, "High yield transfer of ordered nanowire arrays into transparent flexible polymer films," *Nanotechnology*, vol. 23, no. 49, 2012.

[125] L. Wu, S. Li, W. He, D. Teng, K. Wang, and C. Ye, "Automatic release of silicon nanowire arrays with a high integrity for flexible electronic devices," *Sci. Rep.*, vol. 4, pp. 1–7, 2014.

[126] J. M. Weisse, C. H. Lee, D. R. Kim, and X. Zheng, "Fabrication of flexible and vertical silicon nanowire electronics," *Nano Lett.*, vol. 12, no. 6, pp. 3339–3343, 2012.

[127] "First Contact safety data sheet." [Online]. Available: http://www.photoniccleaning.com/v/vspfiles/downloadables/MSDS /PCT First Contact Polymer Solutions SDS All Sizes All Colors ver 1.17 SDS_EU-USA.pdf.

[128] S. F. Leung *et al.*, "Roll-to-roll fabrication of large scale and regular arrays of three-dimensional nanospikes for high efficiency and flexible photovoltaics," *Sci. Rep.*, vol. 4, pp. 1–8, 2014.

[129] D. B. Turner-Evans, H. Emmer, C. T. Chen, and H. A. Atwater, "Flexible, transparent contacts for inorganic nanostructures and thin films," *Adv. Mater.*, vol. 25, no. 29, pp. 4018–4022, 2013.